

Organotypic modeling of SARS-CoV-2 lung and brainstem infection

Marion Ferren (✉ marion.ferren@inserm.fr)

CIRI, Centre International de Recherche en Infectiologie, Team Immunobiology of the Viral infections, Univ Lyon, Inserm, U1111, CNRS, UMR5308, Université Claude Bernard Lyon 1, Ecole Normale Supérieure de Lyon, 69007, LYON, France

Valérie Favede

CIRI, Centre International de Recherche en Infectiologie, Team Immunobiology of the Viral infections, Univ Lyon, Inserm, U1111, CNRS, UMR5308, Université Claude Bernard Lyon 1, Ecole Normale Supérieure de Lyon, 69007, LYON, France

Didier Decimo

CIRI, Centre International de Recherche en Infectiologie, Team Immunobiology of the Viral infections, Univ Lyon, Inserm, U1111, CNRS, UMR5308, Université Claude Bernard Lyon 1, Ecole Normale Supérieure de Lyon, 69007, LYON, France

Mathieu Iampietro

CIRI, Centre International de Recherche en Infectiologie, Team Immunobiology of the Viral infections, Univ Lyon, Inserm, U1111, CNRS, UMR5308, Université Claude Bernard Lyon 1, Ecole Normale Supérieure de Lyon, 69007, LYON, France

Nicole A. P. Lieberman

Department of Laboratory Medicine, University of Washington Medical Center, Seattle, WA, USA

Jean-Luc Weickert

Institut de Génétique et Biologie Moléculaire et Cellulaire, CNRS/INSERM/ULP, Illkirch, France

Rodolphe Pelissier

CIRI, Centre International de Recherche en Infectiologie, Team Immunobiology of the Viral infections, Univ Lyon, Inserm, U1111, CNRS, UMR5308, Université Claude Bernard Lyon 1, Ecole Normale Supérieure de Lyon, 69007, LYON, France

Magalie Mazelier

CIRI, Centre International de Recherche en Infectiologie, Team Immunobiology of the Viral infections, Univ Lyon, Inserm, U1111, CNRS, UMR5308, Université Claude Bernard Lyon 1, Ecole Normale Supérieure de Lyon, 69007, LYON, France

Olivier Terrier

CIRI, Centre International de Recherche en Infectiologie, Team VirPath, Univ Lyon, Inserm, U1111, CNRS, UMR5308, Université Claude Bernard Lyon 1, Ecole Normale Supérieure de Lyon, 69007, LYON, France

Anne Moscona

Center for Host-Pathogen Interaction, Columbia University Medical Center, New York, USA

Matteo Porotto

Center for Host-Pathogen Interaction, Columbia University Medical Center, New York, USA

Alexander L. Greninger

Department of Laboratory Medicine, University of Washington Medical Center, Seattle, WA, USA

Nadia Messaddeq

Institut de Génétique et Biologie Moléculaire et Cellulaire, CNRS/INSERM/ULP, Illkirch, France

Branka Horvat

CIRI, Centre International de Recherche en Infectiologie, Team Immunobiology of the Viral infections, Univ Lyon, Inserm, U1111, CNRS, UMR5308, Université Claude Bernard Lyon 1, Ecole Normale Supérieure de Lyon, 69007, LYON, France

Cyrille Mathieu (✉ cyrille.mathieu@inserm.fr)

CIRI, Centre International de Recherche en Infectiologie, Team Immunobiology of the Viral infections, Univ Lyon, Inserm, U1111, CNRS, UMR5308, Université Claude Bernard Lyon 1, Ecole Normale Supérieure de Lyon, 69007, LYON, France <https://orcid.org/0000-0002-6682-2029>

Research Article

Keywords: SARS-CoV-2, hamster, ex vivo, brainstem, lung, early tropism, innate immune response, cell death

Posted Date: December 10th, 2020

DOI: <https://doi.org/10.21203/rs.3.rs-122126/v1>

License: © ⓘ This work is licensed under a Creative Commons Attribution 4.0 International License. [Read Full License](#)

Abstract

SARS-CoV-2 has caused a global pandemic of Covid-19 since its emergence in December 2019. The infection causes a severe acute respiratory syndrome and may also lead to central nervous system infection and neurological sequelae. We developed and characterized two new organotypic cultures from hamster brainstem and lung tissues that offer the unique opportunity to study the early steps of the pathogenesis and screening of antivirals. Using these models, we validated the early tropism of the virus in the lung and demonstrated that SARS-CoV2 can infect brainstem and cerebellum, mainly by targeting granular neurons. Viral infection induced specific interferon and innate immune responses with patterns specific to each organ along with apoptotic, necroptotic, and pyroptotic cell death. Overall, our data illustrate the potential of rapidly modeling complex tissue level interactions of viral infection in a newly emerged virus.

Introduction

In late 2019, the emergence of the severe acute respiratory syndrome coronavirus 2 (SARS-CoV-2) led to a global pandemic of COVID-19. In November 2020, more than 53 million confirmed cases were reported and more than 1.3 million patients died over the world from this disease¹. SARS-CoV-2 infection induces a severe acute respiratory syndrome which can also be associated with central nervous system (CNS) infection and neurological symptoms including smell dysfunction, headache, muscle pain, myopathy, and in rare cases, generalized myoclonus, ischemic stroke and perivascular acute disseminated encephalomyelitis²⁻⁴. It has been suggested that brainstem infection may be involved in both respiratory and heart failure in patients⁵⁻⁷. To date the neuro-invasive potential of SARS-CoV-2 in human is still poorly understood^{8,9}.

SARS-CoV-2 is an enveloped, positive-sense, single stranded RNA virus that belongs to the *Betacoronavirus* genus within the *Coronaviridae* family. The infection starts with attachment of the viral surface glycoprotein, Spike (S), to the human angiotensin converting enzyme 2 (ACE2) at the surface of the target cell¹⁰. To execute its functions, S must be in its protease-cleaved form, composed of S1 and S2 subunits. The activity of the cellular transmembrane serine protease TMPRSS2 highly correlates with viral dissemination, suggesting that it may participate in processing of S, but S can also be cleaved by the endosomal proteases Cathepsin B and Cathepsin L¹¹. Additionally, cell entry of SARS-CoV-2 can be preactivated by the proprotein convertase furin, reducing the virus's dependence on target cell proteases for entry^{12,13}.

Most observations of the pathogenesis of SARS-CoV-2 infection arise either from *in vitro* or *post mortem* analyses of infected patients, and there is a need for models that will help decipher the initial steps of infection in real time.

Golden Syrian hamsters have been shown to be a relevant small animal model for several viruses¹⁴ and more specifically for respiratory viruses that also target the CNS such as the paramyxoviruses Nipah virus (NiV)¹⁵ and measles virus (MeV)¹⁶. The pathogenesis of SARS-CoV^{17,18} and SARS-CoV-2¹⁹⁻²² infection in Syrian hamsters is similar to that observed in humans, supporting the use of hamster as a model to study SARS-CoV-2 pathogenesis²⁰. Cerebellar and hippocampus organotypic cultures from small rodent models have been characterized in the laboratory and shown to be relevant for studying CNS infection by neurotropic viruses and screening antiviral drugs²³. These *ex vivo* cultures offer the unique opportunity of direct access to the infected

organ in order to address tropism early in infection. In this study we characterize two new 3-dimensional (3D) organotypic culture models obtained from suckling hamster brainstem and lungs, and compare SARS-CoV-2 infection with two neuro-invasive respiratory viruses (NiV and MeV) in lung and brainstem *ex vivo* models.

Both organotypic systems retained their relevant physiological properties for the duration of the experiment (4 days) and were susceptible to NiV and SARS-CoV-2 infection, while in contrast a hyperfusogenic encephalitic MeV strain infected only the brain organotypic cultures. Type 1 and type 2 pneumocytes, as well as ciliated cells, are susceptible to the infection in hamster lung explant cultures, reflecting what has been shown in humans²⁴. In the hamster brainstem, we show that SARS-CoV-2 targets the granular neurons. As part of originality, the interferon and innate immune responses, as well as the associated cell death signatures during the first days of SARS-CoV-2 infection were characterized in real time in both organs.

Results

Hamster lung and brainstem ex vivo cultures are viable and susceptible to for SARS-CoV-2 infection.

Since SARS-CoV-2 mainly targets lungs, and may also infect the brainstem, we have developed new *ex vivo* models of these organs from naive suckling hamsters, based on our previous experience organotypic cerebellum cultures²³. Lung and brainstems were isolated and sliced, at 500 μm and 350 μm thickness respectively, based on the stability of each structure in the slicing process. The 3-dimensional cultures were then maintained on a polytetrafluoroethylene (PTFE) membrane in order to maintain an air-liquid interface for up to 4 days (Fig. 1a). The metabolic activity, the main parameter reflecting viability of the cultures, did not decrease over time as quantified by Alamar blue assay (Fig. 1B). To evaluate the permissiveness of *ex vivo* cultures to SARS-CoV2 infection, we quantified the activity of the entry receptor and the expression level of the proteases known to cleave and mature the virus surface Spike glycoprotein (S) as well as of the virus receptor ACE2. The ACE2 activity/ μg of total protein lysate from hamster organs on the day of slice preparation was assessed in the lung and brainstem cultures and compared to cerebellum cultures used as a reference. ACE2 inhibitor was used to confirm that the quantified activity was real. The three cultures were found to exhibit a similar ACE2 activity, with the lung displaying a slightly higher activity (Fig. 1c). The transcription level of TMPRSS2 and Cathepsin B mRNA, two proteases known to cleave and activate SARS-CoV-2 S, were quantified in cultures by RT-qPCR. As in human tissues, TMPRSS2 was highly expressed in hamster lung but at very low level in brainstem and cerebellum. On the contrary, Cathepsin B mRNA expression level was significantly higher ($\approx 2 \times 10^6$ mRNA copies/ μg of RNA) in the brain cultures compared to the lung (3.6×10^5 mRNA copies/ μg of RNA) (Fig. 1d). These results suggest that the lung organotypic model harbor all main components required for SARS-CoV-2 infection while the brain derived models express fewer TMPRSS2 and might be less permissive to SARS-CoV-2 infection.

Organotypic cultures are susceptible to SARS-CoV-2 infection

In order to evaluate the infectability of these new models, hamster lungs, brainstem (and cerebellum) organotypic cultures were infected with recombinant SARS-CoV-2_neon green (icSARS-CoV-2-mNG). In parallel, to compare the permissiveness of the organotypic cultures with other encephalitic respiratory viruses, the

cultures were also infected with recombinant Nipah virus (NiV) and measles virus (MeV), both expressing enhanced green fluorescent protein (EGFP) (referred to as rNiV-EGFP and MeV IC323-EGFP-F L454W, a CNS adapted MeV that can infect in the absence of known receptors²⁵, respectively). Viral entry (Fig. 2a,b,c) and dissemination (Extended Data Fig. 1) were followed by microscopy at day 1 and 4 days post infection (dpi). Interestingly, icSARS-CoV-2-mNG and NiV-EGFP entered and disseminated in both lung and brain cultures (Fig. 2a,b and Extended Data Fig. 1) whereas MeV IC323-EGFP-F L454W only infected the brainstem and the cerebellum (Fig. 2c and Extended Data Fig. 1). Even at 4 dpi the hyperfusogenic MeV did not infect any cells in the lung cultures, suggesting that MeV entry in lung epithelial cells may require additional factors in this model (Fig. 2c and Extended Data Fig. 1). SARS-CoV2 infection was then followed by genome quantification by RT-qPCR. The viral load was higher in lung than in brainstem and cerebellum (Fig. 2d). This difference was already observed on the day of infection (Fig. 2d). The greater susceptibility of lung cultures might arise either from the thickness of the slice (thicker than that of the brainstem and cerebellum cultures) or perhaps from a greater number of ACE2 expressing cells (as supported by the slightly higher ACE2 activity (Fig. 1c). In the lung, the viral replication was very fast and the number of SARS-CoV-2 genomes/ μg of RNA almost reached the plateau after 1 dpi (1.2×10^8 genomes/ μg of RNA). In the brainstem and cerebellum, the replication was delayed, with an increase in genome copies being observed only after 2 days, and reached values lower than those in the lung (Fig. 2d). Altogether, these results show that all analyzed *ex vivo* cultures are susceptible to the SARS-CoV-2 infection, although with the slightly different kinetics.

SARS-CoV-2 infection can be blocked by Remdesivir in organotypic lung and brainstem cultures

Remdesivir is in clinical use for COVID-19^{26–28} and we used it to validate our models for drug evaluation. The slices were treated daily at two different concentrations of Remdesivir starting two hours after infection (Fig. 2e). After 4 days of treatment the metabolic activity of both lung and brainstem remained very close to 100% and to that of non-treated slices, suggesting the very low, not to say null, effect on metabolic activity of the drug at these doses (Fig. 2f). The lower dose (2 μM) of Remdesivir did not have a significant inhibitory effect on infection as assessed by RT-qPCR. However, after treatment with 10 μM of Remdesivir, infection was reduced by almost 100% at 4 dpi in both lung and brainstem. These data confirm utility of these models for assessing drugs prior to *in vivo* experiments.

SARS-CoV-2 preferentially targets neurons in brain, and ciliated cells, type 1 and type 2 pneumocytes in lungs

To evaluate which cells are the main to be targeted, viral tropism was evaluated by transmission electron microscopy (TEM) in lung and brainstem organotypic cultures, followed by immunofluorescent staining analyzed by confocal microscopy (Fig. 3). Based on the kinetics of virus replication, all the organotypic cultures shown in figures.3 and 4 were collected at 1 dpi for the lung and at 2 dpi for the brainstem and cerebellum. In lung cultures infection was observed in type 1 and type 2 pneumocytes, as well as in the ciliated cells from the general area of the bronchioles (Fig. 3a,b,c). The immunofluorescence analysis confirmed these observations by showing the presence of SARS-CoV-2_S staining in cells positive for surfactant protein C (SP-C), Aquaporin 5 (AQP5) and α acetylated Tubulin (Tub) staining that are specific for type 2, type 1

pneumocytes and ciliated cells, respectively (Fig. 3d,e,f). Most of the cells display microvillae as expected in young animals (Fig. 3c and Extended Data Fig. 2a). Infected cells harbored a large number of vacuoles and showed multiple signs of cell degradation: cytoplasmic material degradation, membrane coiling (blue star), large empty vacuoles (green arrow) (Fig. 3b1,b2). We observed autophagosomal vacuoles containing virions or degraded viral particles in all types of infected cells (Fig. 3a,b,c,g and Extended Data Fig. 2c). Virions were also found attached on the microvillae outside the cells (Extended Data Fig. 2a) and several cells showed disorganization of the smooth endoplasmic reticulum (SER), as well as accumulation of lipids and mitochondria that were undergoing degradation (Extended Data Fig. 2b).

In the brainstem and in the cerebellum, the TEM analysis showed viruses in granular neurons (Fig. 3g and Extended Data Fig. 2d) with a developed Golgi apparatus. Moreover, the viral particles are often localized in double-membraned vacuoles (red arrows) inside the cells where other Coronavirus are generally observed during their cell cycle (Fig. 3g1,g2)^{29,30}. In the immunofluorescence analysis, SARS-CoV-2_S staining colocalized with NeuN positive cells (Fig. 3h), confirming the infection of granular neurons. Myelin Basic Protein (MBP) staining surrounds the SARS-CoV-2_S without colocalization, suggesting that the cells positive for the infection could also be myelinated neurons and not oligodendrocytes (Fig. 3i). The cultures were also stained for microglia marker (Iba1), astrocytes (GFAP) and Olig2 (used as a second marker for oligodendrocytes) and SARS-CoV-2_S staining was not found in these cells (Fig. 3i,j,k). In the cerebellum, the TEM analysis showed the infection of Golgi neurons with viral particles in autophagosomes. We did not observe infection of Purkinje neurons (Extended Data Fig. 2d1,d2), suggesting that under these conditions there is a selective infection of specific neuronal subtypes by SARS-CoV-2.

SARS-CoV-2 in these models infects almost all epithelial lung cells, but is selective for neuronal subtypes in the CNS. In both lungs and brain organotypic cultures, the infection led to a marked cell degeneration that could conceivably affect organ functions.

Apoptotic, necroptotic and pyroptotic signatures are detected in both organotypic cultures

Since unbalanced inflammatory responses can provoke organ failure, we evaluated cell death signatures in the SARS-CoV-2-infected organotypic cultures. First, we performed TEM analysis which highlighted the presence of apoptotic and necrotic cellular disorders in both infected lungs and brainstem (Fig. 4a,b). The involvement of apoptosis was verified by TUNEL assays in both organotypic cultures (Fig. 4c,d). TUNEL staining was observed similarly in both non infected and infected cultures, potentially due to the experimental procedure (data not shown). However, most of the cells positive for SARS-CoV-2 staining were not positive for TUNEL, confirming that apoptotic cell death observed by TEM might not be the direct consequence of viral infection. Alternatively, the cell death related to viral infection may be caspase-independent (Fig. 4c,d). Using RT-qPCR we corroborated necroptotic events in line with microscopic observations despite an erratic expression of Tumor Necrosis Factor α (TNF α) throughout the 4 days of infection (Fig. 4f). Indeed, we observed in both cultures a sharp increase in Mixed Lineage Kinase Domain Like Pseudokinase (MLKL) mRNA levels (Fig. 4e) which is known to be associated with Caspase 8 deficiency and Inflammatory Bowel Disease commonly observed in patients. Moreover, we showed that pyroptosis also occurs during viral infection as inferred from the increase in Gasdermin D mRNA levels in both infected lungs and brainstem cultures (Fig. 4g). Gasdermin D is also known

to be substrate of inflammation-related caspases, thus imbalancing inflammatory response potentially leading to organ failure^{31,32}. Interestingly, whereas Gasdermin D levels decreased at day 4 post-infection in the lungs, its expression kept increasing in the brainstem, possibly due to a difference in infection kinetics between both tissues. Furthermore, while the levels of Interleukin 18 (IL-18) mRNA remained low in both organotypic cultures (Fig. 4h), we documented a difference in the expression of Interleukin 1 β (IL-1 β) mRNA that increased in the brainstem while it remained low in the lungs (Fig. 4i). These data reveal that distinct cellular mechanisms lead to pyroptosis in the two organs.

Innate and inflammatory responses are increased in both organotypic cultures

To characterize the recapitulation of the responses of these models to SARS-CoV-2 infection, we transcriptomically profiled infected and uninfected organotypic cultures of both hamster brainstem and lungs (Fig. 5a,b,c,d). The transcriptomic first level of analysis pointed out the strong stimulation of the immune response with 19 and 20 out of 20 mainly altered Gene Ontology (GO) categories related to immunity in lung and brainstem respectively (Fig. 5a,b). Alternatively, eight GO categories related to lymphocyte responses were altered in brainstem versus two in lung. To go further, the dichotomy in cellular responses occurring in both tissues at day 4 post-infection was confirmed by the gene expression patterns, highlighting organ-dependent specificities in the host response to the infection (Fig. 5c,d). Indeed, the most significantly differentially expressed genes (DEG) in the lung include a plethora of upregulated interferon-stimulated genes (Fig. 5c), while these significant DEG brainstem conversely contained many downregulated neuronal markers (Fig. 5d). This is consistent with the observation that the percentage of polyadenylated transcripts aligning to the SARS-CoV-2 genome is 6.74 fold higher in lung than brainstem (2.90% vs 0.43%) (Fig. 5c,d).

In parallel, specific immunological markers including Myxovirus Resistance 1 (MX1), Interferon Stimulated Exonuclease Gene 20 (ISG20), C-X-C Motif Chemokine Ligand 10 (CXCL10) and C-C Motif Chemokine Ligand 5 (CCL5) mRNA were quantified by RT-qPCR (Fig. 5e,f,g,h). However, specific genes encoding interferon-stimulated genes (ISG) or chemokines were similarly upregulated in both organotypic cultures, pointing to these as potentially relevant to the innate immune response. Indeed, RT-qPCR profiles showed that the expression of MX1 and ISG20 ISGs and of CCL5 and CXCL10 chemokines were increased within the 4 days kinetics following SARS-CoV-2 infection in both cultures. Interestingly, ISG20 mRNA amounts decreased rapidly to lower levels determining that its reducing antiviral exonuclease activity may be compensated at later time (Fig. 5f). Moreover, while exhibiting a similar trend, we noticed that all those responses were delayed in brain cultures compared to lung ones (Fig. 5e,f,g,h).

Discussion

SARS-CoV-2 infection starts in the lung, inducing a severe acute respiratory syndrome regularly associated with neurological symptoms. While the CNS involvement has been the topic of extensive study, little attention has been paid to the possible role of brainstem infection in organ failure. In the ventral medulla oblongata, the preBötzing complex is a defined neural network that is critical for generating respiratory rhythm³³. Whether it

is infected in human remains to be determined, however it is plausible that brainstem infection during the acute phase of the infection could affect both respiratory and heart function⁵⁻⁷.

Organotypic cultures offer an opportunity to follow early steps of infection in real time in a native 3D multicellular context³⁴. Non-standardized lung *ex vivo* slices have been used for respiratory virus pathogenesis studies in multiple host species (from mice to monkeys)^{35,36}. The highly standardized lung organotypic cultures we describe can be extended to several small animal models. Organotypic brainstem cultures have been previously characterized using 3 to 18 days old mice or rats; with a focus on brain development, neuronal respiratory networks and neurodegenerative diseases³⁷⁻⁴⁰. Our study provides a first characterization of these models for the first 4 days of infection. From a single animal we can prepare a large number of organotypic cultures (*e.g.*, ≈ 8 from brainstem, ≈ 20 from lung and up to ≈ 10 from cerebellum) allowing for numerous comparisons to be carried out in real time and simultaneously on several organs. The system is complementary to human airway epithelia that are used for preliminary screening^{26,41}, since organotypic cultures are a more complex organ-like system to assess antiviral drugs prior to *in vivo* work. As such, they complement the human airway epithelial system, also a 3D lung model grown at an air-liquid interface, that has been recently used to evaluate SARS-CoV-2 antiviral molecules⁴².

The use of viruses encoding a fluorescent protein allows monitoring of the infection in real time within tissues. In distinction to SARS-CoV infection, it remains unclear whether SARS-CoV-2 targets the brain. Our data show that SARS-CoV-2 infects and spreads in the brain (Fig. 2).

Our brainstem cultures derive mainly from the medulla and the pons for the top-central part⁴³. SARS-CoV-2 seems to target specific locations in the pons and in the medulla; the motor and sensory areas respectively.

We observed green fluorescence in the zone of X and XII cranial nerve (CN) fibers, which are responsible for motor (CN X and CN XII) and sensory functions (CN X). In the cerebellar cultures, infection starts from the deep nucleus and the thin layer of granular cells (Fig. 2).

Interestingly, NiV and MeV infect quite different areas, and more extensively, possibly related to their broader tropism in the CNS. This underlines the interest of organotypic cultures to reveal cell specificity of different viral infections, not previously observed in infections *in vivo*.

The lung organotypic cultures were found to be highly specific for respiratory tract tropic viruses. The neurotropic MeV IC323-EGFP-F L454W did not infect these cultures, in line with our previous studies showing that similarly hyperfusogenic neurotropic variants are generally found in the brain⁴⁴. We found that ACE2 activity per μg of total protein was similar in the lung and the brain, with the caveat that the assay does not specify which cells express the receptor and to what extent (Fig. 1). On the contrary TMPRSS2 expression in the brain tissues was lower than in the lungs. Cathepsin B expression was similar in the two organs. In

addition, while cathepsin B can replace TMPRSS2 for S cleavage⁴⁵, it may not be as efficient as TMPRSS2. We suggest that a lower level of host protease activity in the brain may contribute to the delayed infection. A more technical explanation is that lung cultures are larger and thicker than brainstem cultures and may contain a broader range of infectable cells, accounting for the higher concentration of viral RNA after two hours (Fig. 2).

In human lung, ACE2 expression concentrates at the surface of lung alveolar epithelial cells, mainly on type I and type II pneumocytes but also in bronchial epithelial cells⁴⁶. In hamster organotypic lung culture model ciliated cells, type 1 and type 2 pneumocytes are infected (Fig. 3). Our findings are consistent with other *in vivo* SARS-CoV-2 studies in hamsters that revealed inflammation and severe lesions in the lung with infection of the bronchiolar epithelial cells, type I and II pneumocytes^{20,22}. We also found viral clusters in autophagosomes confirming the conservation of this observation between infected species (Fig. 3). In bronchial human airway epithelium (HAE) apically infected with SARS-CoV-2, TEM analysis also highlighted double-membrane vesicles and spherule containing virions⁴⁷.

Several studies have shown that SARS-CoV-2 can infect neurons from human induced pluripotent stem cells derived brain organoids⁴⁸⁻⁵⁰. In hamsters, viral antigens are commonly observed in olfactory neurons, but very few or none in the brain parenchyma while the virus can be recover from brain of 1 month old infected animal^{21,22}. These data suggest that the virus may have limited capacity to cross the blood brain barrier. Here, we show that neurons from hamster brainstem and cerebellum can be infected by SARS-CoV-2 (Fig. 3). NeuN staining revealed infection of granular neurons as observed by the TEM analysis, likely to be Golgi II neurons (Fig. 3g,h). Interestingly, we came to the same conclusion in cerebellum cultures in which we did not detect any infection in Purkinje neurons (Extended Data Fig. 2). While ACE2 expression has been described in neurons and glial cells we did not see any infection in the oligodendrocytes neither cell body, nor myelin fibers, however myelinated neurons were infected⁵¹. These results suggest a specific early tropism for neurons in the CNS, in distinction to the broader range of cells targeted in the lungs.

At the intracellular level, infected lung and brain cultures revealed numerous vacuoles, cytoplasm material degradation, mark of stress, membrane coiling and disorganized Golgi apparatus, evidence of cell degeneration or death. Cell death has been evaluated in SARS-CoV-2 infected organs *in vivo* (*i.e.* in hamster lungs) and in neurons from human brain organoids^{20,50}. Our experiments revealed that apoptosis, necroptosis and pyroptosis occurred during SARS-CoV-2 infection in both lung and brainstem (Fig. 4). Apoptosis was directly observed in both lung and brainstem cells via TEM analysis (Fig. 4), and TUNEL assays showed that very few cells undergoing apoptosis were infected, suggesting that apoptosis may occur through indirect stimuli. Necroptosis, a cell death mechanism involving TNF α stimuli^{52,53}, appeared in both organotypic cultures, consistent with the uncontrolled expression of TNF α and high levels of MLKL mRNA we found throughout the 4 days of infection in both the lungs and brainstem. The signature of pyroptosis emerged in both *ex vivo* systems, with high levels of GasderminD mRNA. However, as already reported, pyroptosis can be triggered through two distinct pathways, one through direct pathogen recognition and IL-1 β ⁵⁴, the second one

via activation of ST2 receptors by IL-33⁵⁵. The discordant results we obtained for IL-1 β mRNA between the brainstem and the lungs demonstrate tissue-dependent pyroptosis. While IL-18 mRNA copy number remained low in both organs, brainstem underwent a large increase in IL-1 β mRNA levels that are known to be associated with GasderminD involvement⁵⁶. In contrast, in the lungs, while GasderminD mRNA increased, the levels of IL-1 β mRNA remained low, demonstrating that the lung-associated pyroptosis operates differently than in the brainstem.

In support of this hypothesis, a previous study demonstrated that high levels of IL-33 were released and ST2 receptors signaling pathways were highly triggered during infection of epithelial airway tissues, provoking further pyroptosis⁵⁷. Altogether, our observations suggest that tissue-associated cell death induced following SARS-CoV-2 infection in both organs could be the result of distinct dysregulated inflammatory responses.

The IFN-I and IFN-III responses were triggered in various *in vitro* and *in vivo* models during SARS-CoV-2 infection^{58,59}. We confirmed these results in our *ex vivo* organotypic cultures, showing an increase of both IFN-I and IFN-III-triggered interferon stimulated genes ISG20 and Mx1 mRNA levels, mainly involved in establishing optimal antiviral and inflammatory environments when their expressions are correctly balanced (Fig. 5).

In parallel, we demonstrated increased mRNA levels for CXCL10 and CCL5, attractant chemokines that recruit inflammatory mediators. As expected from the delay in the start of viral replication, the dynamics of these responses were delayed in brainstem compared to the lung, confirming differences in cell susceptibility to viral infection in both tissues.

Conclusions

In this study we characterize two *ex vivo* models to establish their utility for the investigation of infectious pathogens. We demonstrate that organotypic lung and brainstem cultures are relevant 3D physiological models for several human viral infections including SARS-CoV-2, and will be useful for assessment of antiviral drugs. The models will also lend themselves to real time evaluation of emerging mutants. SARS-CoV-2 infected type 1 and type 2 pneumocytes and ciliated cells in the lung, and granular and Golgi neurons in brain structures.

Expression of ACE2, TMPRSS2 and Cathepsin B in organotypic cultures was consistent with the *in vivo* distribution of SARS-CoV-2 during the first 4 days of infection. We highlight a correlation between TMPRSS2 expression levels and a delay in CNS infection at the level of the organs, which could offer the innate immune system a window of opportunity for preventing CNS infection. Once SARS-CoV-2 reaches the brain, virus infects specific neurons in the brainstem and cerebellum potentially involved in respiratory and cardiac function. We described the induction of type I and III innate immune responses and the inflammatory response to infection at the organ level. Finally, in both organotypic cultures, we observed cell death caused by the infection via caspase-3 independent apoptosis, necroptosis and pyroptosis. Taken together these results pave the way for the use of these models to study SARS-CoV-2 pathogenesis and assess efficacy of candidate antivirals before *in vivo* validation.

Declarations

Acknowledgments

The Fig. 1a has been created with BioRender.com.

We thank Bruno Lina, Andres Pizzorno and Manuel Rosa-Calatrava from the CIRI, Centre International de Recherche en Infectiologie, LYON, France, for providing us with the BetaCoV/France/IDF0571/2020 virus. We acknowledge World Reference Center for Emerging Viruses and Arboviruses (WRCEVA) and UTMB investigator, Dr. Pei Yong Shi for kindly providing recombinant icSARS-CoV-2-mNG virus based on 2019-nCoV/USA_WA1/2020 isolate.

We thank Sonia Longhi from AFMB UMR 7257, CNRS and Aix-Marseille University, France, and Frédéric Carrière from BIP UMR 7281, CNRS and Aix-Marseille University, France, for advice and help in proofreading of the manuscript. We acknowledge Denis Gerlier for helpful advices and critical reading of the manuscript. We thank Fabienne Archer for providing us with anti-SP-C and anti- α Tubulin antibodies and for her numerous precious advices.

We thank Géraldine Gourru-Lesimple and Claire Dumont for assistance in lab management.

This work was supported by ANR-CoronaPepStop (ANR-20-COVI-000) and Fondation de France to BH and ANRS-COV8-SARSRhinCell to CM.

Author Contributions

Conceptualization, M.F., C.M., D.D. and M.I.; Methodology, M.F. and C.M. ; Formal Analysis, M.F., N.A.P.L. and N.M.; Investigation, M.F., D.D., V.F., M.M., J.L.W. and R.P.; Resources, O.T.; Writing – Original Draft, M.F., C.M. and M.I.; Writing – Review & Editing, A.M., A.L.G., M.P., N.M., O.T. and B.H.; Supervision, C.M.

Declaration of Interests

The authors declare no competing interests.

Methods

Viruses. BetaCoV/France/IDF0571/2020 virus (GISAID Accession ID = EPI_ISL_411218) was isolated in Vero E6 from a nasal swab of one of the first COVID-19 positive patient in France⁶¹ and was kindly given by Virpath lab.

2019-nCoV/USA_WA1/2020 virus was isolated by the CDC in the United States, from the first patient diagnosed in the US.

The recombinant NeonGreen SARS-CoV-2 virus (icSARS-CoV-2-mNG) has been generated by introducing Neon Green reporter gene into ORF7 of the viral genome as described elsewhere ⁶².

The recombinant Measles virus (MeV IC323-EGFP-F L454W) is an hyperfusogenic MeV variant able to disseminate in absence of known receptor ⁶³. This variant is expressing the gene encoding EGFP and was generated using reverse genetics in 293-3-46 cells as previously described ⁶⁴ after modification of the plasmid encoding MeV IC323-EGFP (kindly provided by Yanagi, Kyushu University, Fukuyoka, Japan).

The recombinant Nipah virus (rNiV-EGFP) is expressing the gene encoding the EGFP and was generated using reverse genetic in 293 cells and prepared as previously described ⁶⁵. NiV infections were carried out at the INSERM Jean Mérieux BSL4 laboratory in Lyon, France.

All viruses have been produced and titrated at 37°C in Vero E6 cells (SARS-CoV-2 and rNiV-EGFP viruses) or in Vero E6 expressing human SLAM receptor (MeV IC323-EGFP-F L454W). Briefly, for stock production, cells were infected with MOI=0.01 in DMEM. After 90min incubation at 37°C, medium was replaced with DMEM-2% FBS (SARS-CoV-2) or medium was added in order to obtain DMEM-5% FBS (rNiV-EGFP and MeV IC323-EGFP-F L454W) and the cells were incubated at 37°C in 5% CO₂ atmosphere for two days. Viral supernatant were collected and centrifuged (400xg, 5min), aliquoted and titrated in plaque forming unit by classic dilution limit assay.

Alamar blue assay. The organotypic cultures (n=6) were immersed in 200µl of 1X Alamarblue® (Invitrogen; DAL1025) solution in culture medium during 2 hours at 37°C in a humidified atmosphere in 5% CO₂. The fluorescence was read in a 96-well white plate using 560/590 nm (ex/em) filter settings according to the manufacturer's protocol.

ACE2 activity assay. The ACE2 enzymatic activity was quantified using 100µg of organotypic cultures (n=3) using the Angiotensin II Converting Enzyme (ACE2) Activity Assay Kit (Fluorometric) (CliniSciences; K897-100) and following the manufacturer recommendations. Total protein was quantified using the Micro BCA Protein Assay Kit (Thermo Fisher Scientific).

Organotypic culture preparation and treatment. Organotypic cultures were prepared from suckling Hamsters (*Mesocricetus auratus*, Janvier lab) and maintained in culture as detailed elsewhere (welsh 2017). Briefly, organ substructures (i.e. cerebellum, brainstem, left lung) were isolated from 7-day-old animals (n=5; sex non-discriminated) and cut with a McIlwain tissue chopper (WPI-Europe) : 350-µm-thick progressive slices for brainstem and cerebella, and 500-µm-thick slices for lung. The cultures were then separated from each other in cold Hibernate®-A/5 g/L D-Glucose/1x Kynurenic acid buffer and laid out on hydrophilic polytetrafluoroethylene cell culture insert membranes (PICM0RG50, Millipore). Slices were subsequently cultured in Minimal Essential Medium GlutaMAX supplemented with 25% horse serum, 5 g/L glucose, 1% HEPES (all Thermo Fisher Scientific), and 0.1 mg/L human recombinant insulin (Sigma-Aldrich) at 37°C in 5% CO₂. The medium was changed every other day after the slicing procedure. Slices from 5 hamsters were infected on the day of slicing with SARS-CoV-2 (BetaCoV/France/IDF0571/2020), icSARS-CoV-2-mNG ⁶², MeV IC323-EGFP-F L454W and rNiV-eGFP. For the treatment, cultures were then treated from 90min post infection to day 4 post infection either with Remdesivir (GS-5734; Clinisciences) diluted in Neurobasal medium or with

vehicle (untreated condition) once a day for the 10 μ M dose and twice a day for the 2 μ M condition. 2 μ l of 100 μ M or 20 μ M of Remdesivir were added on top of each of the 5 slices in each well and the Remdesivir concentration in the feeding medium was also adjusted in order to reach a final concentration of 10 μ M or 2 μ M in the insert. At each time point, slices were collected, and the RNA were extracted in order to perform RT-qPCR.

RNA Extraction and quantitative RT-PCR. Total RNA from organotypic cultures were extracted using the NucleoSpin RNA Kit (Macherey-Nagel) and quantified by spectrophotometer (DS-11-FX , DeNovix). For an upcoming SARS-CoV-2 genome quantification, 100ng of total RNA were reverse transcribed using the SuperScript™ III Reverse Transcriptase (Invitrogen) with the SARS-CoV2_tagged primer: 5'-gcaggcaatctcacaatcaggGGTCTGCATGAGTTTAGG-3'. To improve specificity of the RT-qPCR we have opted for a specific reverse transcription using a primer specific to the genome tagged with a Nipah virus (NiV) derived sequence. The qPCR step uses then a reverse primer against SARS-CoV-2 and a forward primer against NiV extension.

For the GAPDH (Glyceraldehyde 3-phosphate dehydrogenase) and all other genes, 100ng of total RNA were reverse transcribed using the iScript cDNA Synthesis Kit (Bio-Rad). Obtained cDNAs were diluted 1:10. Quantitative PCR was performed using Platinum SYBR Green qPCR SuperMix-UDG (Invitrogen) on a StepOnePlus Real-Time PCR System (Applied Biosystems). Primers were either designed using Beacon Designer (version 8) software or chosen after validation that their efficacy was close to 100% according to the MIQE checklist ⁶⁶. All samples were run in duplicate and results were analyzed using StepOne version 2.3 (Applied Biosystems). All results were normalized to the standard deviation (SD) for GAPDH mRNA, and the calculations were performed using the $2^{\Delta\Delta CT}$ model ⁶⁷. For each time point, fold change are relative to the number of copies of mRNAs in infected organotypic cultures compared to the uninfected ones.

Table 1: Oligonucleotides used for RT-qPCR

| Gene | Primer forward | Primer reverse |
|--------------------------|---|---------------------------|
| Hamster_Gapdh | GCATGGCCTTCCGTGTCC | TGTCATCATACTTGGCAGGTTTCT |
| SARS-CoV-2 genome | GCAGGGCAATCTCACAATCAGG (NiV extension) | CGCATACAAAACATTCCC |
| SARS-CoV-2 Nucleoprotein | AAACATTCCCACCAACAG | CACTGCTCATGGATTGTT |
| Hamster_MX1 | CTTCAAGGAGCACCCACACT | CTTGCCCTCTGGTGACTCTC |
| Hamster_TNFa | TGAGCCATCGTGCCAATG | AGCCCGTCTGCTGGTATCAC |
| Hamster_IL6 | GGACAATGACTATGTGTTGTTAGAA | AGGCAAATTTCCCAATTGTATCCAG |
| Hamster_CXCL10 | AGACAACAGTAACTCCAGTGACAAG | AGTGTAGCACCTCAGCGTAGC |
| Hamster_IL1b | TGGACCTTCCAGGATGAGGACA | GTTTATCTCGGAGCCTGTAGTG |
| Hamster_IL18 | AATGACCCTGGCTGCATTAC | CCAGCATGGGGAGAACTAAA |
| Hamster_Gasdermin D | AACAGGTGACCACGGAAGAC | TGCTGGGTTGGTCATGTAAA |
| Hamster_MLKL | ATCAAGTTTTGCTCGGTGCT | GTGCCTGTATTCCCAGCATT |
| Hamster_ISG20 | TGCAGCATTGTGAACTTCAGTG | GCAGGATCTCTAGTCTGGCTTC |
| Hamster_CCL5 | ACTGCCTCGTGTTACATCA | CCCCTTCTTCTTTGGGTTG |
| Hamster_Cathepsin B | GCTGTAATGGTGGCTATC | AGGGAGGTATGGTGTATG |
| Hamster_TMPRSS2 | CTCACTGTGTGGAAGAAC | CTTGGTCTCAGAGTTGTAAT |

Organotypic cultures RNA-Seq and analysis. RNA from uninfected and infected hamster organotypic cultures (pool of 5 slices) was collected and extracted as described above and submitted to the JP Sulzberger Columbia Genome Center for library preparation and sequencing. Strand-specific RNA-Seq libraries were prepared using a poly-A enrichment and were sequenced on an Illumina NovaSeq 6000 with paired end 2x100 reads (Nextera xt kit; Illumina). After quality and adapter trimming with Trimmomatic v0.39⁶⁸, transcript abundance quantification was performed using Kallisto version 0.46.0⁶⁹ with the Ensembl *Mesocricetus auratus* v1.0 as the reference genome.

Differential gene expression analysis was performed using the Kallisto transcript abundances and the R Bioconductor package DESeq2⁷⁰. In lung cultures, 262 genes out of 15870 expressed genes were differentially expressed (DE) at a threshold of absolute value of log₂ fold change > 2. In brain stem cultures, 170/16041 expressed genes were differentially expressed. Code for analysis is available at https://github.com/greninger-lab/SARS-CoV-2_hamster_RNAseq.

Because the hamster genome remains relatively poorly annotated, Gene Ontology (GO) analysis was performed using mouse annotations to test for statistical enrichment of DE genes in GO categories. After exclusion of genes that did not have a mouse ortholog, 195 DE genes out of 11726 were analyzed in lung, and 125/12698 in brainstem, using the R package clusterProfiler⁷¹. For each tissue, the 20 non-redundant GO categories with the lowest adjusted p value for Fisher exact test of enrichment were displayed using ggplot⁷².

To calculate % reads on target for SARS-CoV-2 reads each sample was aligned against the EPI_ISL_411218 SARS-CoV-2 reference sequence using Bowtie2 with default parameters⁷³. SARS-CoV-2 on target percentages were calculated using the number of mapped reads in the resulting BAM file.

Heatmaps were generated using the R package pheatmap by calculating the log₂fold change for infected samples relative to uninfected samples and taking the 50 with the largest absolute value, after eliminating those in which there were fewer than 5 normalized counts in the uninfected sample for lung, or 1 in brain. Genes for which the annotation did not include a formal gene symbol were manually searched in the Ensembl database for highly conserved rodent orthologues, which are included next to the Ensembl gene name in the heatmaps.

Immunofluorescent stainings. Organotypic cultures from seven days-old hamsters were infected with 1,000 PFU of BetaCoV/France/IDF0571/2020 virus. 24 hours post infection the slices were fixed during 1 hour in 4% paraformaldehyde (PFA), washed in 1× Dulbecco's phosphate-buffered saline (DPBS) and permeabilized and blocked in 1× DPBS-3% BSA-0.3% Triton X-100 (perm and block solution) overnight at 4°C. Slices were incubated in the perm and block solution containing the primary antibodies overnight at 4°C. After 3 washes (5 min each) in 1× DPBS, slices were incubated in the perm and block solution containing the secondary antibodies for 1 h at RT; donkey anti-rabbit conjugated with Alexa 488 or 555, donkey anti-mouse conjugated with Alexa 488 or 555, and donkey anti-goat conjugated with Alexa 555 or 647 antibodies (1:500 each). After 3 washes in 1× DPBS, slices were mounted with Fluoromount-G® aqueous mounting medium (SouthernBiotech, catalog no. 0100-01) on epoxy slides (CEL-LINE, catalog no. 30-12A-BLACK-CE24) and coverslipped. Images were taken using an inverted microscope Zeiss Axio Observer.Z1 with confocal unit LSM 800 and analyzed using ImageJ software.

TUNEL assay. TUNEL assay (Click-iT™ Plus TUNEL Assay for In Situ Apoptosis Detection, Alexa Fluor™ 647 dye, ThermoFisher Scientific) was performed following the manufacturer recommendations.

Transmission electron microscopy. Infected organotypic cultures were fixed by immersion in 2.5% glutaraldehyde (Sigma) and 2.5% Paraformaldehyde in cacodylate buffer (0.1M, pH 7.2) at 4°C for several days. The samples were post fixed in 1% osmium tetroxyde in 0.1M Cacodylate buffer for 1 hour at 4°C, and rinsed with Cacodylate buffer 0.1M (2x10min) and with water (2x10min) and immersed in uranyl acetate at 4% for 2 h at 4°C. Samples were dehydrated through graded alcohol (50, 70, 90 and 100%) and propylene oxide for 30 min each and embedded in Epon™ 812 (Sigma-Aldrich, Saint-Louis, Missouri, USA). Semi-thin sections were cut at 2 µm with an ultra-microtome (Leica Ultracut UCT) and stained with 1% Toluidine blue in 1% sodium borate, examined by Leica optical microscope (LEICA DMLB, Leica Microsystems GmbH; Germany). Ultrathin sections were cut at 70nm and contrasted with uranyl acetate and lead citrate and

examined at 70kv with a Morgagni 268D electron microscope (FEI Electron Optics, Eindhoven, and the Netherlands). Images were captured digitally by Mega View III camera (Soft Imaging System).

Statistical analysis. Statistical analyses for Figs. 1 and 2 were performed using the Kruskal-Wallis test. ***, $P < 0.001$. For the Figs. 4 and 5, statistical analyses were performed using the Mann-Whitney test and the One sample T-test. *, $P < 0.05$; **, $P < 0.01$; ***, $P < 0.001$. All statistical analysis were performed in GraphPad Prism5 software.

References

1. Worldometer. Coronavirus Cases. *Worldometer* 1–22 (2020). doi:10.1101/2020.01.23.20018549V2
2. Orsucci, D., Ienco, E. C., Nocita, G., Napolitano, A. & Vista, M. Neurological features of COVID-19 and their treatment: A review. *Drugs in Context* **9**, (2020).
3. Khoo, A. *et al.* Postinfectious brainstem encephalitis associated with SARS-CoV-2. *J. Neurol. Neurosurg. Psychiatry* **91**, jnnp-2020-323816 (2020).
4. Rábano-Suárez, P. *et al.* Generalized myoclonus in COVID-19. *Neurology* **95**, 10.1212/WNL.0000000000009829 (2020).
5. Chigr, F., Merzouki, M. & Najimi, M. Comment on “The neuroinvasive potential of SARS-CoV-2 may play a role in the respiratory failure of COVID-19 patients”. *Journal of Medical Virology* **92**, 703–704 (2020).
6. Li, Y. C., Bai, W. Z. & Hashikawa, T. The neuroinvasive potential of SARS-CoV2 may play a role in the respiratory failure of COVID-19 patients. *Journal of Medical Virology* **92**, 552–555 (2020).
7. Smith, J. C., Ellenberger, H. H., Ballanyi, K., Richter, D. W. & Feldman, J. L. Pre-Bötzinger complex: A brainstem region that may generate respiratory rhythm in mammals. *Science (80-)*. **254**, 726–729 (1991).
8. Liu, K., Pan, M., Xiao, Z. & Xu, X. Neurological manifestations of the coronavirus (SARS-CoV-2) pandemic 2019-2020. *Journal of Neurology, Neurosurgery and Psychiatry* **91**, 669–670 (2020).
9. Bulfamante, G. *et al.* First ultrastructural autoptoc findings of sars-cov-2 in olfactory pathways and brainstem. *Minerva Anestesiologica* **86**, 678–679 (2020).
10. Zhou, P. *et al.* A pneumonia outbreak associated with a new coronavirus of probable bat origin. *Nature* **579**, 270–273 (2020).
11. Hoffmann, M. *et al.* SARS-CoV-2 Cell Entry Depends on ACE2 and TMPRSS2 and Is Blocked by a Clinically Proven Protease Inhibitor. *Cell* **181**, 271-280.e8 (2020).
12. Coutard, B. *et al.* The spike glycoprotein of the new coronavirus 2019-nCoV contains a furin-like cleavage site absent in CoV of the same clade. *Antiviral Res.* **176**, (2020).
13. Shang, J. *et al.* Cell entry mechanisms of SARS-CoV-2. *Proc. Natl. Acad. Sci. U. S. A.* **117**, (2020).
14. Miao, J., Chard, L. S., Wang, Z. & Wang, Y. Syrian Hamster as an Animal Model for the Study on Infectious Diseases. *Frontiers in Immunology* **10**, (2019).
15. Wong, K. T. *et al.* A golden hamster model for human acute Nipah virus infection. *Am. J. Pathol.* **163**, 2127–37 (2003).

16. Watanabe, S. *et al.* Mutant fusion proteins with enhanced fusion activity promote measles virus spread in human neuronal cells and brains of suckling hamsters. *J. Virol.* **87**, 2648–2659 (2013).
17. Roberts, A. *et al.* Severe Acute Respiratory Syndrome Coronavirus Infection of Golden Syrian Hamsters. *J. Virol.* **79**, 503–511 (2005).
18. Roberts, A. *et al.* Animal models and vaccines for SARS-CoV infection. *Virus Res.* **133**, 20–32 (2008).
19. Imai, M. *et al.* Syrian hamsters as a small animal model for SARS-CoV-2 infection and countermeasure development. *Proc. Natl. Acad. Sci. U. S. A.* **117**, 16587–16595 (2020).
20. Chan, J. F. W. *et al.* Simulation of the clinical and pathological manifestations of Coronavirus Disease 2019 (COVID-19) in golden Syrian hamster model: implications for disease pathogenesis and transmissibility. *Clin. Infect. Dis.* (2020). doi:10.1093/cid/ciaa325
21. Bryche, B. *et al.* Massive transient damage of the olfactory epithelium associated with infection of sustentacular cells by SARS-CoV-2 in golden Syrian hamsters. *Brain. Behav. Immun.* (2020). doi:10.1016/j.bbi.2020.06.032
22. Sia, S. F. *et al.* Pathogenesis and transmission of SARS-CoV-2 in golden hamsters. *Nature* **583**, 834–838 (2020).
23. Welsch, J. *et al.* Organotypic Brain Cultures: A Framework for Studying CNS Infection by Neurotropic Viruses and Screening Antiviral Drugs. *Bio-protocol* **7**, (2017).
24. Gkogkou, E., Barnasas, G., Vougas, K. & Trougakos, I. P. Expression profiling meta-analysis of ACE2 and TMPRSS2, the putative anti-inflammatory receptor and priming protease of SARS-CoV-2 in human cells, and identification of putative modulators. *Redox Biol.* **36**, 101615 (2020).
25. Jurgens, E. M. *et al.* Measles fusion machinery is dysregulated in neuropathogenic variants. *MBio* **6**, 1–12 (2015).
26. Pizzorno, A. *et al.* In vitro evaluation of antiviral activity of single and combined repurposable drugs against SARS-CoV-2. *Antiviral Res.* **181**, (2020).
27. Wang, Y. *et al.* Remdesivir in adults with severe COVID-19: a randomised, double-blind, placebo-controlled, multicentre trial. *Lancet* **395**, 1569–1578 (2020).
28. Beigel, J. H. *et al.* Remdesivir for the Treatment of Covid-19 – Final Report. *N. Engl. J. Med.* (2020). doi:10.1056/nejmoa2007764
29. Miller, S. & Krijnse-Locker, J. Modification of intracellular membrane structures for virus replication. *Nature Reviews Microbiology* **6**, 363–374 (2008).
30. Snijder, E. J. *et al.* Ultrastructure and Origin of Membrane Vesicles Associated with the Severe Acute Respiratory Syndrome Coronavirus Replication Complex. *J. Virol.* **80**, 5927–5940 (2006).
31. Lieberman, J., Wu, H. & Kagan, J. C. Gasdermin D activity in inflammation and host defense. *Sci. Immunol.* **4**, (2019).
32. de Vasconcelos, N. M., Van Opdenbosch, N., Van Gorp, H., Parthoens, E. & Lamkanfi, M. Single-cell analysis of pyroptosis dynamics reveals conserved GSDMD-mediated subcellular events that precede plasma membrane rupture. *Cell Death Differ.* **26**, 146–161 (2019).
33. Viemari, J. C., Menuet, C. & Hilaire, G. Complexe de pré-Bötzinger et automatisme respiratoire Identification électrophysiologique, molculaire et gntique dune structure cruciale pour la respiration. *Medecine/Sciences*

- 29, 875–882 (2013).
34. Welsch, J. C. *et al.* Type I Interferon Receptor Signaling Drives Selective Permissiveness of Astrocytes and Microglia to Measles Virus during Brain Infection. *J. Virol.* **93**, (2019).
 35. de Vries, R., Rennick, L., Duprex, W. & de Swart, R. Paramyxovirus Infections in Ex Vivo Lung Slice Cultures of Different Host Species. *Methods Protoc.* **1**, 12 (2018).
 36. Nguyen, D. T. *et al.* Paramyxovirus infections in ex vivo lung slice cultures of different host species. *J. Virol. Methods* **193**, 159–165 (2013).
 37. Forsberg, D. *et al.* CO₂-evoked release of PGE₂ modulates sighs and inspiration as demonstrated in brainstem organotypic culture. *Elife* **5**, (2016).
 38. Phillips, W. S., Herly, M., Del Negro, C. A. & Rekling, J. C. Organotypic slice cultures containing the preBötzing complex generate respiratory-like rhythms. *J. Neurophysiol.* **115**, 1063–1070 (2016).
 39. Cavaliere, F., Vicente, E. S. & Matute, C. An organotypic culture model to study nigro-striatal degeneration. *J. Neurosci. Methods* **188**, 205–212 (2010).
 40. Busceti, C. L. *et al.* Corticosterone upregulates gene and protein expression of catecholamine markers in organotypic brainstem cultures. *Int. J. Mol. Sci.* **20**, (2019).
 41. Han, Y. *et al.* Identification of Candidate COVID-19 Therapeutics using hPSC-derived Lung Organoids. *bioRxiv Prepr. Serv. Biol.* (2020). doi:10.1101/2020.05.05.079095
 42. Outlaw, V. K. *et al.* Inhibition of Coronavirus Entry In Vitro and Ex Vivo by a Lipid-Conjugated Peptide Derived from the SARS-CoV-2 Spike Glycoprotein HRC Domain. *MBio* **11**, (2020).
 43. atlas.brain-map.org. Interactive Atlas Viewer: Atlas Viewer. Available at: <http://atlas.brain-map.org/atlas?atlas=1#atlas=1&plate=100960184&structure=987&x=4526&y=4727.25&zoom=-4&resolution=16.75&z=6>. (Accessed: 26th August 2020)
 44. Ferren, M., Horvat, B. & Mathieu, C. Measles encephalitis: Towards new therapeutics. *Viruses* **11**, 1017 (2019).
 45. Heurich, A. *et al.* TMPRSS2 and ADAM17 Cleave ACE2 Differentially and Only Proteolysis by TMPRSS2 Augments Entry Driven by the Severe Acute Respiratory Syndrome Coronavirus Spike Protein. *J. Virol.* **88**, 1293–1307 (2014).
 46. Hamming, I. *et al.* Tissue distribution of ACE2 protein, the functional receptor for SARS coronavirus. A first step in understanding SARS pathogenesis. *J. Pathol.* **203**, 631–637 (2004).
 47. Pizzorno, A. *et al.* Characterization and Treatment of SARS-CoV-2 in Nasal and Bronchial Human Airway Epithelia. *Cell Reports Med.* **1**, 100059 (2020).
 48. Zhang, B. Z. *et al.* SARS-CoV-2 infects human neural progenitor cells and brain organoids. *Cell Research* 1–4 (2020). doi:10.1038/s41422-020-0390-x
 49. Song, E. *et al.* Neuroinvasive potential of SARS-CoV-2 revealed in a human brain organoid model. *bioRxiv* 2020.06.25.169946 (2020). doi:10.1101/2020.06.25.169946
 50. Ramani, A. *et al.* SARS-CoV-2 targets neurons of 3D human brain organoids. *EMBO J.* (2020). doi:10.15252/embj.2020106230
 51. Baig, A. M., Khaleeq, A., Ali, U. & Syeda, H. Evidence of the COVID-19 Virus Targeting the CNS: Tissue Distribution, Host-Virus Interaction, and Proposed Neurotropic Mechanisms. *ACS Chemical Neuroscience*

- 11**, 995–998 (2020).
52. Christofferson, D. E. & Yuan, J. Necroptosis as an alternative form of programmed cell death. *Current Opinion in Cell Biology* **22**, 263–268 (2010).
53. Vandenabeele, P., Galluzzi, L., Vanden Berghe, T. & Kroemer, G. Molecular mechanisms of necroptosis: An ordered cellular explosion. *Nature Reviews Molecular Cell Biology* **11**, 700–714 (2010).
54. Fink, S. L. & Cookson, B. T. Caspase-1-dependent pore formation during pyroptosis leads to osmotic lysis of infected host macrophages. *J. Immunol.* **202**, 1913–1926 (2006).
55. Cohen, E. S. *et al.* Oxidation of the alarmin IL-33 regulates ST2-dependent inflammation. *Nat. Commun.* **6**, (2015).
56. Liu, X. *et al.* Inflammasome-activated gasdermin D causes pyroptosis by forming membrane pores. *Nature* **535**, 153–158 (2016).
57. Yagami, A. *et al.* IL-33 Mediates Inflammatory Responses in Human Lung Tissue Cells. *J. Immunol.* **185**, 5743–5750 (2010).
58. Lokugamage, K. *et al.* Type I interferon susceptibility distinguishes SARS-CoV-2 from SARS-CoV. *bioRxiv Prepr. Serv. Biol.* (2020). doi:10.1101/2020.03.07.982264
59. Stanifer, M. L. *et al.* Critical Role of Type III Interferon in Controlling SARS-CoV-2 Infection in Human Intestinal Epithelial Cells. *Cell Rep.* **32**, (2020).
60. Preibisch, S., Saalfeld, S. & Tomancak, P. Globally optimal stitching of tiled 3D microscopic image acquisitions. *Bioinformatics* **25**, 1463–1465 (2009).
61. Lescure, F. X. *et al.* Clinical and virological data of the first cases of COVID-19 in Europe: a case series. *Lancet Infect. Dis.* **20**, 697–706 (2020).
62. Xie, X. *et al.* An Infectious cDNA Clone of SARS-CoV-2. *Cell Host Microbe* **27**, 841-848.e3 (2020).
63. Mathieu, C. *et al.* Measles Virus Bearing Measles Inclusion Body Encephalitis-Derived Fusion Protein Is Pathogenic after Infection via the Respiratory Route. *J. Virol.* **93**, (2019).
64. Radecke, F. *et al.* Rescue of measles viruses from cloned DNA. *EMBO J.* **14**, 5773–84 (1995).
65. Yoneda, M. *et al.* Establishment of a Nipah virus rescue system. *Proc. Natl. Acad. Sci. U. S. A.* **103**, 16508–16513 (2006).
66. Bustin, S. A. *et al.* The MIQE Guidelines: Minimum Information for Publication of Quantitative Real-Time PCR Experiments. *Clin. Chem.* **55**, 611–622 (2009).
67. Pfaffl, M. W. A new mathematical model for relative quantification in real-time RT-PCR. *Nucleic Acids Res.* **29**, (2001).
68. Bolger, A. M., Lohse, M. & Usadel, B. Trimmomatic: A flexible trimmer for Illumina sequence data. *Bioinformatics* **30**, 2114–2120 (2014).
69. Bray, N. L., Pimentel, H., Melsted, P. & Pachter, L. Near-optimal probabilistic RNA-seq quantification. *Nat. Biotechnol.* **34**, 525–527 (2016).
70. Love, M. I., Huber, W. & Anders, S. Moderated estimation of fold change and dispersion for RNA-seq data with DESeq2. *Genome Biol.* **15**, (2014).
71. Yu, G., Wang, L. G., Han, Y. & He, Q. Y. ClusterProfiler: An R package for comparing biological themes among gene clusters. *Omi. A J. Integr. Biol.* **16**, 284–287 (2012).

72. Wickham, H. Create Elegant Data Visualisations Using the Grammar of Graphics • ggplot2. (2016).

Available at: <https://ggplot2.tidyverse.org/>. (Accessed: 2nd November 2020)

73. Langmead, B. & Salzberg, S. L. Fast gapped-read alignment with Bowtie 2. *Nat. Methods* **9**, 357–359 (2012).

Figures

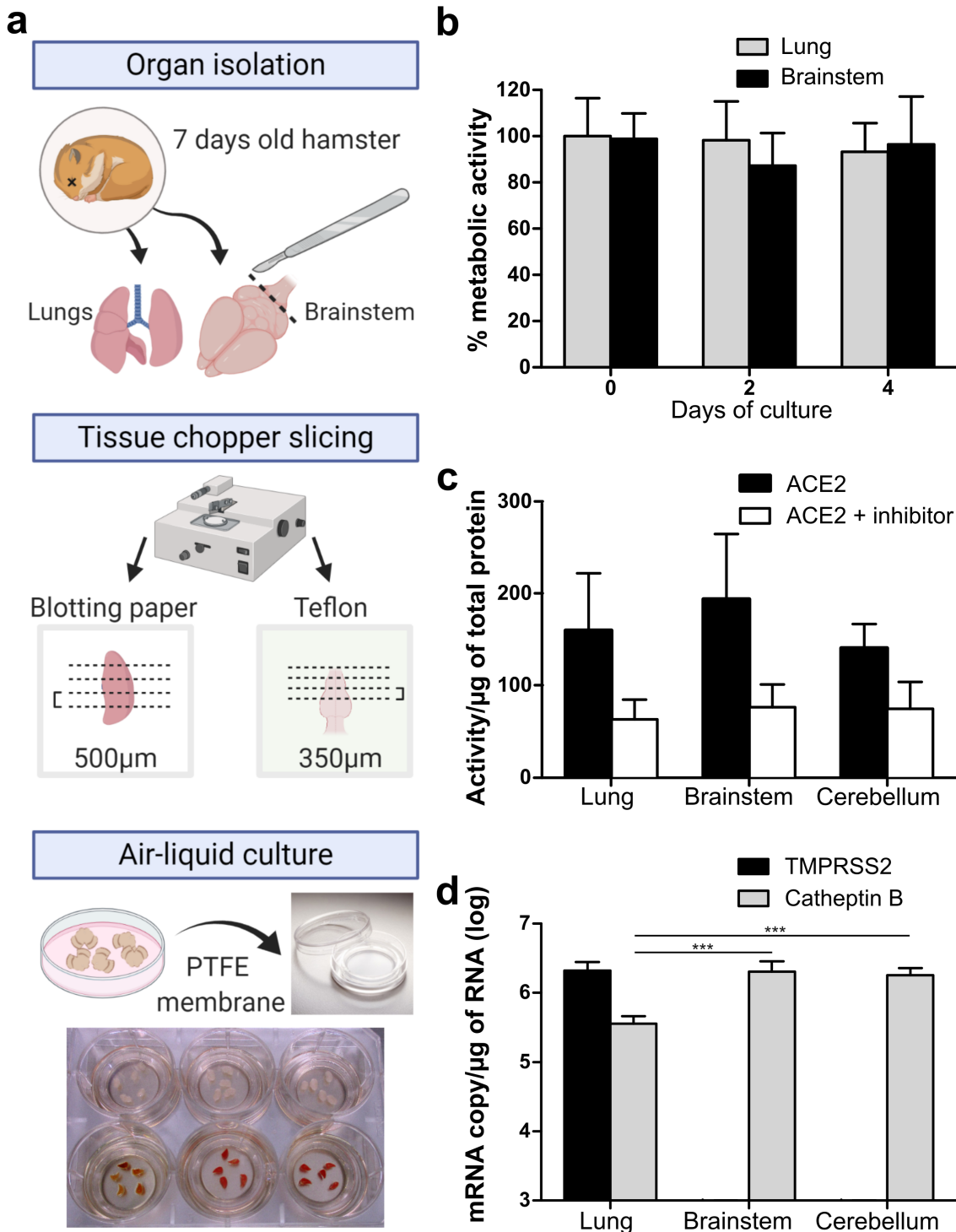


Figure 1

Characterization of the lung and brainstem organotypic cultures. a, Schematic of generation of the hamster organotypic cultures. b, Cellular metabolism activity over time in % of day 0 of culture, quantified by Alamar blue assay. c, ACE2 activity quantified by the fluorometric ACE2 Activity Assay Kit. d, TMPRSS2 and Cathepsin B basal mRNA expression in the models quantified by RT-qPCR (day 0 of culture). Error bars represent SD. Statistical analyses were performed using the Kruskal-Wallis test. ***, $P < 0.001$.

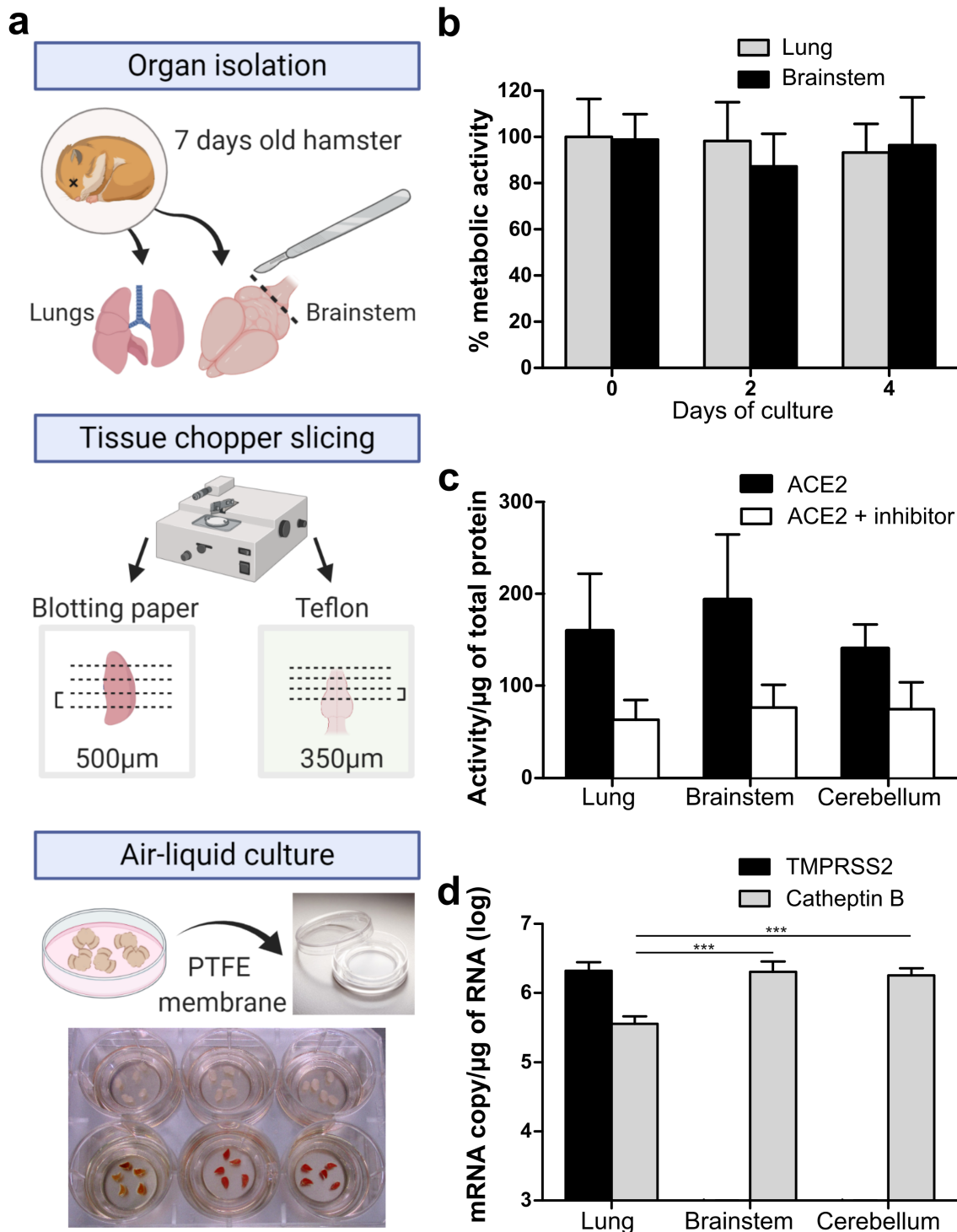


Figure 1

Characterization of the lung and brainstem organotypic cultures. a, Schematic of generation of the hamster organotypic cultures. b, Cellular metabolism activity over time in % of day 0 of culture, quantified by Alamar

blue assay. c, ACE2 activity quantified by the fluorometric ACE2 Activity Assay Kit. d, TMPRSS2 and Cathepsin B basal mRNA expression in the models quantified by RT-qPCR (day 0 of culture). Error bars represent SD. Statistical analyses were performed using the Kruskal-Wallis test. ***, $P < 0.001$.

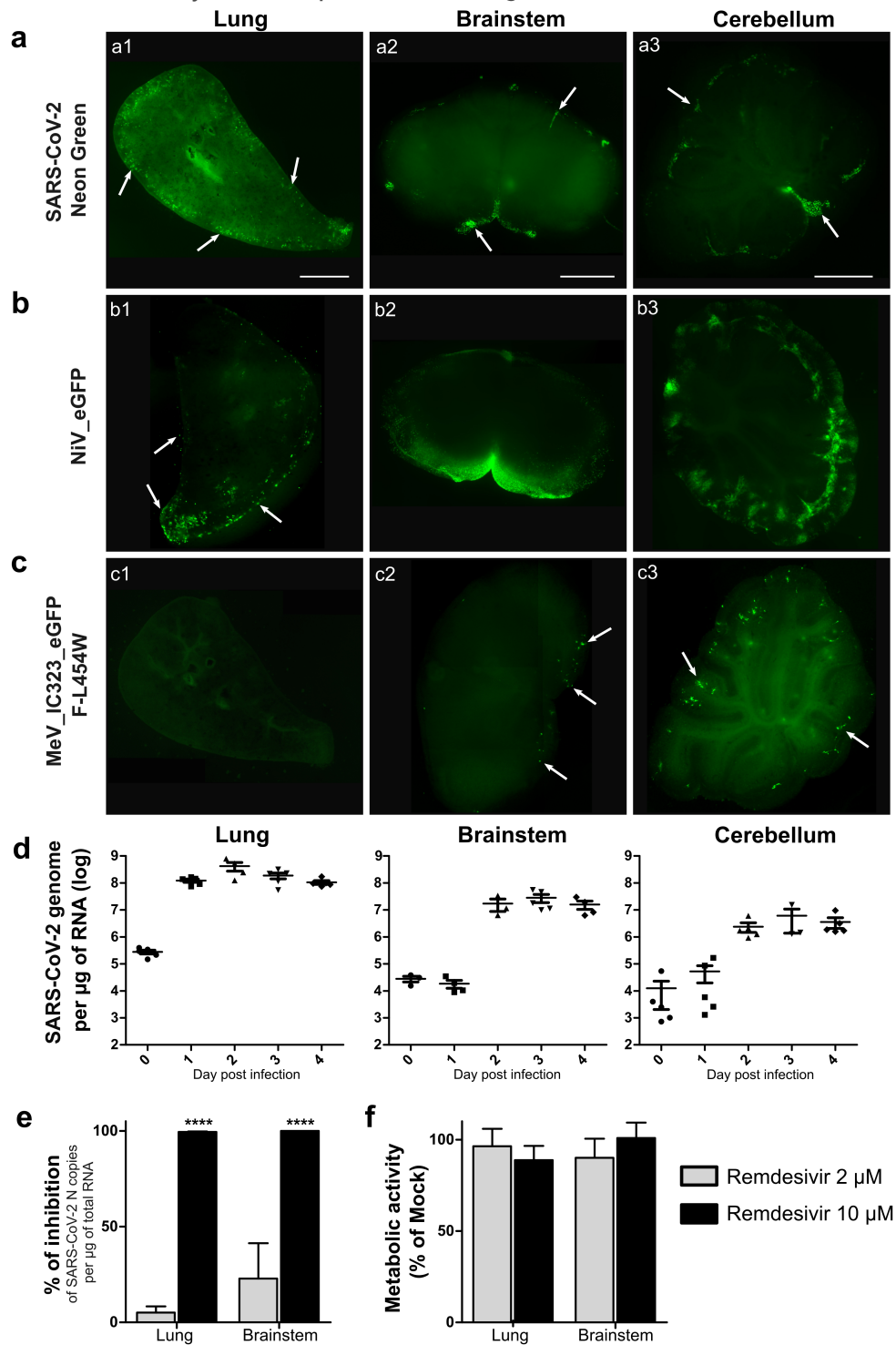


Figure 2

Hamster organotypic cultures infection by three respiratory viruses, dissemination of SARS-CoV-2 and antiviral activity of Remdesivir. a,b,c, The entry of 3 different encephalitogenic respiratory viruses, icSARS-CoV-2-mNG (infection : 1,0000 pfu), NiV-EGFP (infection : 5,000 pfu) and the hyperfusogenic variant MeV IC323-EGFP-F L454W (infection : 1,000 pfu) was monitored by following the fluorescence at 1 dpi (a1,2,3; b1; c1,2,3), or 2 dpi

(b2,3); representative of 2 slices. Pictures were taken using a Nikon Eclipse Ts2R microscope and reconstituted using the Stitching plug-in with ImageJ software 60. Scale bar = 1 mm. d, SARS-CoV-2 genomes per μg of total RNA were quantified by RT-qPCR in lung, brainstem and cerebellum organotypic cultures (n=5) at 90min post infection and 1, 2, 3 and 4 days post infection (dpi) with 5,000 pfu and normalized to the standard deviation for GAPDH mRNA. e, Organotypic cultures from hamsters were infected with SARS-CoV-2 at 1,000 pfu/slice and treated at the indicated concentrations of Remdesivir at 90min, 24, 48 and 72h after infection (n=5). Total RNA was harvested at 4 days post infection and the level of SARS-CoV-2 N gene expression was quantified by RT-qPCR. Results are expressed in % of inhibition of the infection compare to non-treated cultures. Statistical analyses were performed using the Kruskal-Wallis test. ***, $P < 0.001$. f, The toxicity of Remdesivir on uninfected cultures that were treated in the same way was performed by an Alamar blue assay. Results are expressed in percent of metabolic activity after 4 days compare to the non-treated samples. All error bars represent SD.

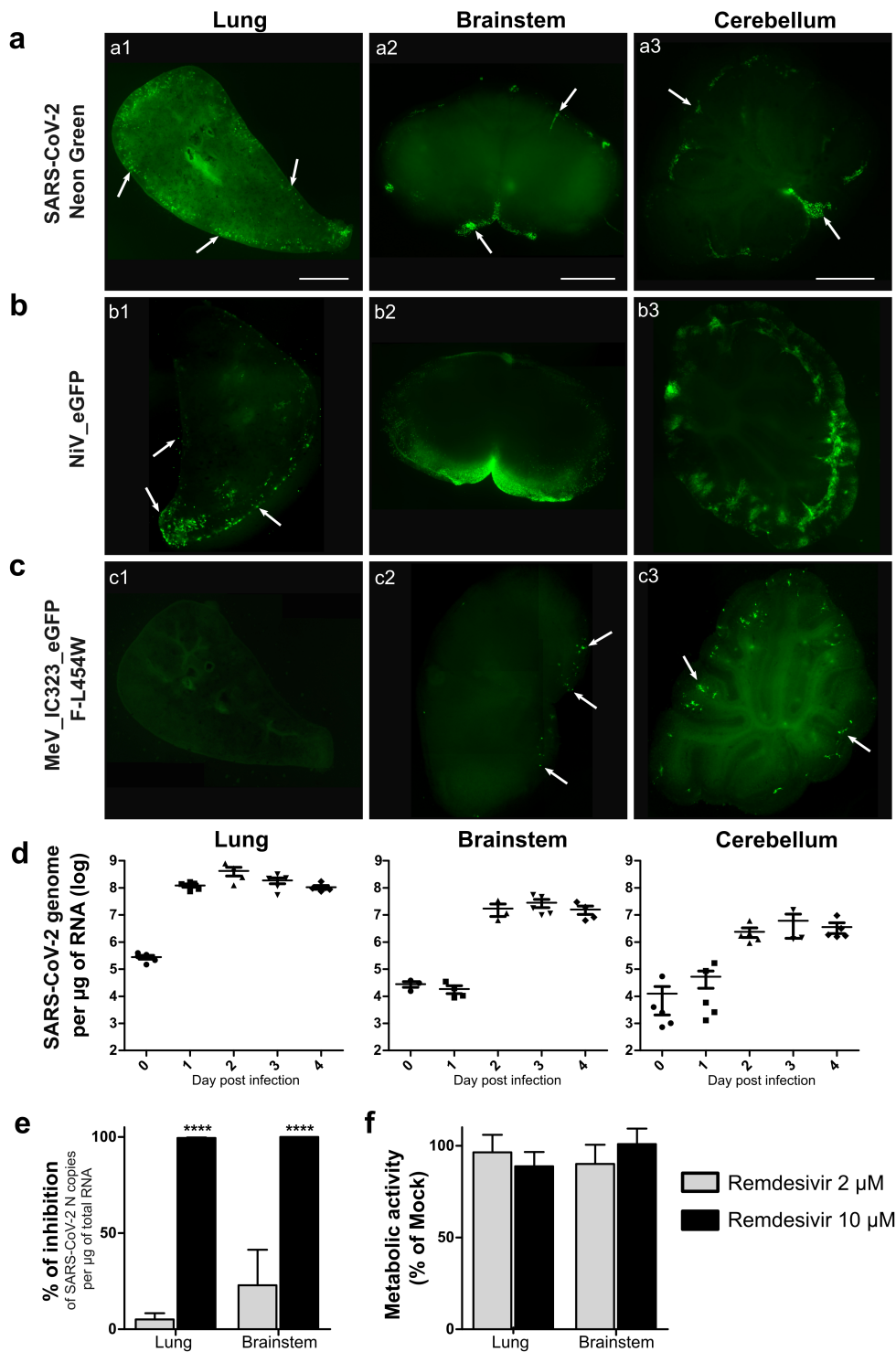


Figure 2

Hamster organotypic cultures infection by three respiratory viruses, dissemination of SARS-CoV-2 and antiviral activity of Remdesivir. a,b,c, The entry of 3 different encephalitogenic respiratory viruses, icSARS-CoV-2-mNG (infection : 1,0000 pfu), NiV-EGFP (infection : 5,000 pfu) and the hyperfusogenic variant MeV IC323-EGFP-F L454W (infection : 1,000 pfu) was monitored by following the fluorescence at 1 dpi (a1,2,3; b1; c1,2,3), or 2 dpi (b2,3); representative of 2 slices. Pictures were taken using a Nikon Eclipse Ts2R microscope and reconstituted using the Stitching plug-in with ImageJ software 60. Scale bar = 1 mm. d, SARS-CoV-2 genomes per μg of total RNA were quantified by RT-qPCR in lung, brainstem and cerebellum organotypic cultures (n=5) at 90min post

infection and 1, 2, 3 and 4 days post infection (dpi) with 5,000 pfu and normalized to the standard deviation for GAPDH mRNA. e, Organotypic cultures from hamsters were infected with SARS-CoV-2 at 1,000 pfu/slice and treated at the indicated concentrations of Remdesivir at 90min, 24, 48 and 72h after infection (n=5). Total RNA was harvested at 4 days post infection and the level of SARS-CoV-2 N gene expression was quantified by RT-qPCR. Results are expressed in % of inhibition of the infection compare to non-treated cultures. Statistical analyses were performed using the Kruskal-Wallis test. ***, P < 0.001. f, The toxicity of Remdesivir on uninfected cultures that were treated in the same way was performed by an Alamar blue assay. Results are expressed in percent of metabolic activity after 4 days compare to the non-treated samples. All error bars represent SD.

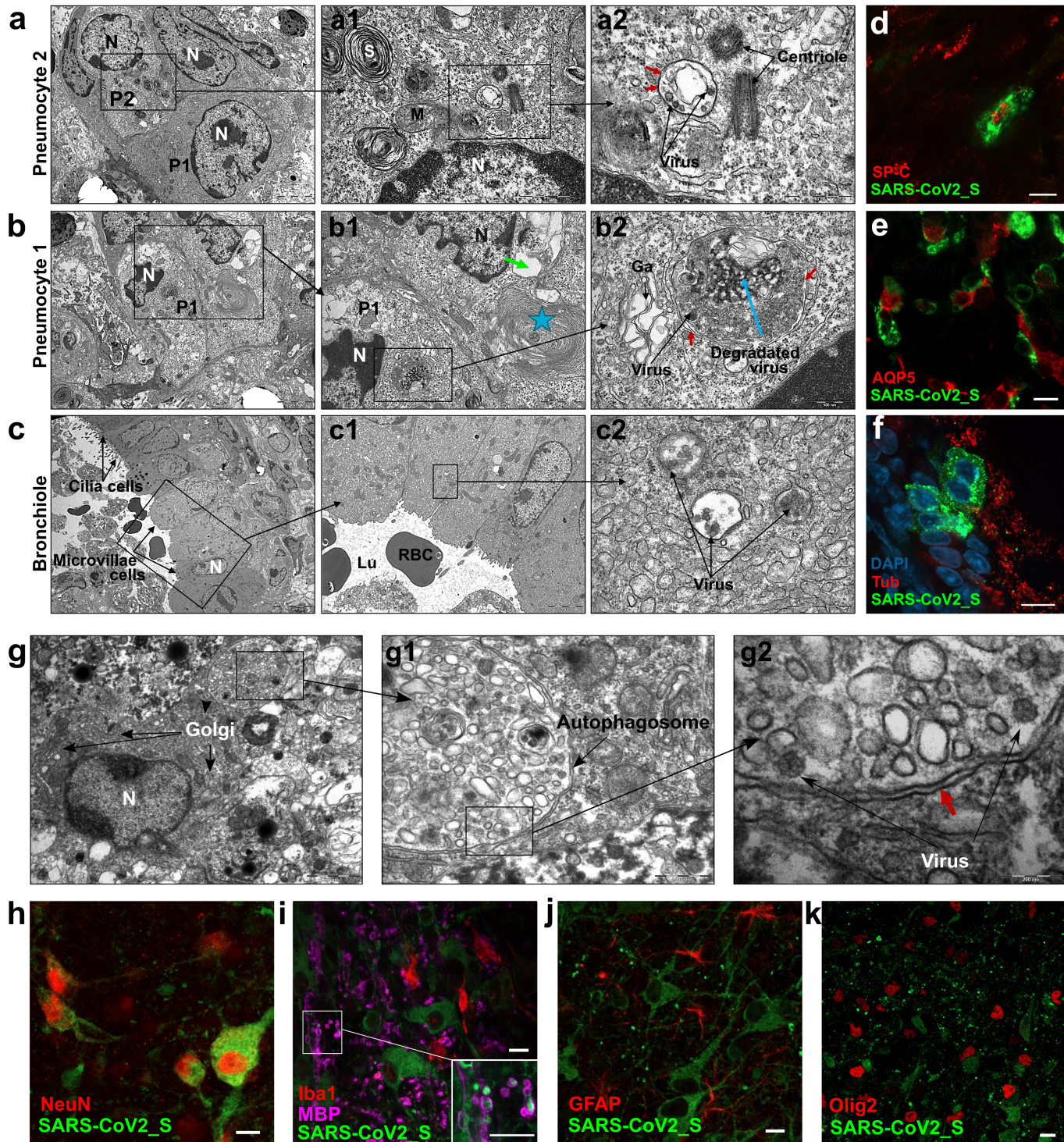


Figure 3

SARS-CoV-2 tropism in hamster lung and brainstem organotypic cultures during the first 2 days of infection. Cultures were infected with 1,000 pfu of SARS-CoV-2 and fixed at day 1 post infection (lung cultures) or 2 days post infection (brainstem cultures). a,b,c, Ultrastructure of infected lung cells by transmission electron microscopy (TEM), scale bar is represented bottom right on each picture. a, Low magnification of lung cells ; P1= type 1 pneumocyte, P2= type 2 pneumocyte, N=nucleus. a1, Enlargement of an infected type 2 pneumocyte with dense lamellar bodies in the cytoplasm (S= surfactant synthesis), a part of the nucleus, the centriole, mitochondria and autophagosomal vacuoles containing virions. a2, High magnification showing the centriole and the autophagosomal vacuole containing virions. Black arrows point to the double membrane. b, Lung cells undergoing degeneration, displaying vacuoles and degraded cytoplasmic material. N=nucleus, P1= type 1 pneumocyte. b1, Enlargement of cells from the Fig. b, P1 cell contains an autophagosome containing virions, several vacuoles and heterochromatine in the nucleus. The second cell exhibits membrane coiling (star) and large empty vacuoles (green arrow), indicating degradation. b2, High magnification showing the double membrane of the autophagosome (red arrows) containing an accumulation of viral material (blue arrow). The black arrow show viruses surrounding the vacuole. Ga= swelled Golgi apparatus. c, Respiratory bronchiole showing ciliated cells and microvillous cells. N=nucleus. c1, Enlargement of the cells from the Fig. c, showing microvillous cells and red blood cells (RBC) in the lumen of the bronchia (Lu). C2 : High magnification showing three autophagosomes containing virions (arrows). d,e,f, Lung cultures were stained with antibodies: anti-SARS-CoV-2_S, d, anti SP-C, e, anti-AQP5 and f, anti- α acetylated Tubulin (Tub). The immunofluorescence staining analysis was performed by confocal microscopy. Scale bar 10 μ m. g, TEM analysis of a brainstem slice showing an infected neuron with a large Golgi apparatus. g1,2, Enlargement of the autophagosome containing viral particles (white arrows). The double membrane of the autophagosome is pointed with the red arrow. h,i,j,k, Brainstem slices stained with antibodies anti-SARS-CoV-2_S, h, anti-NeuN, i, anti-Myelin Basic Protein (MBP) and Iba1, i, anti-GFAP and j, anti-Olig2. The immunofluorescence staining analysis was performed by confocal microscopy. Scale bar 10 μ m.

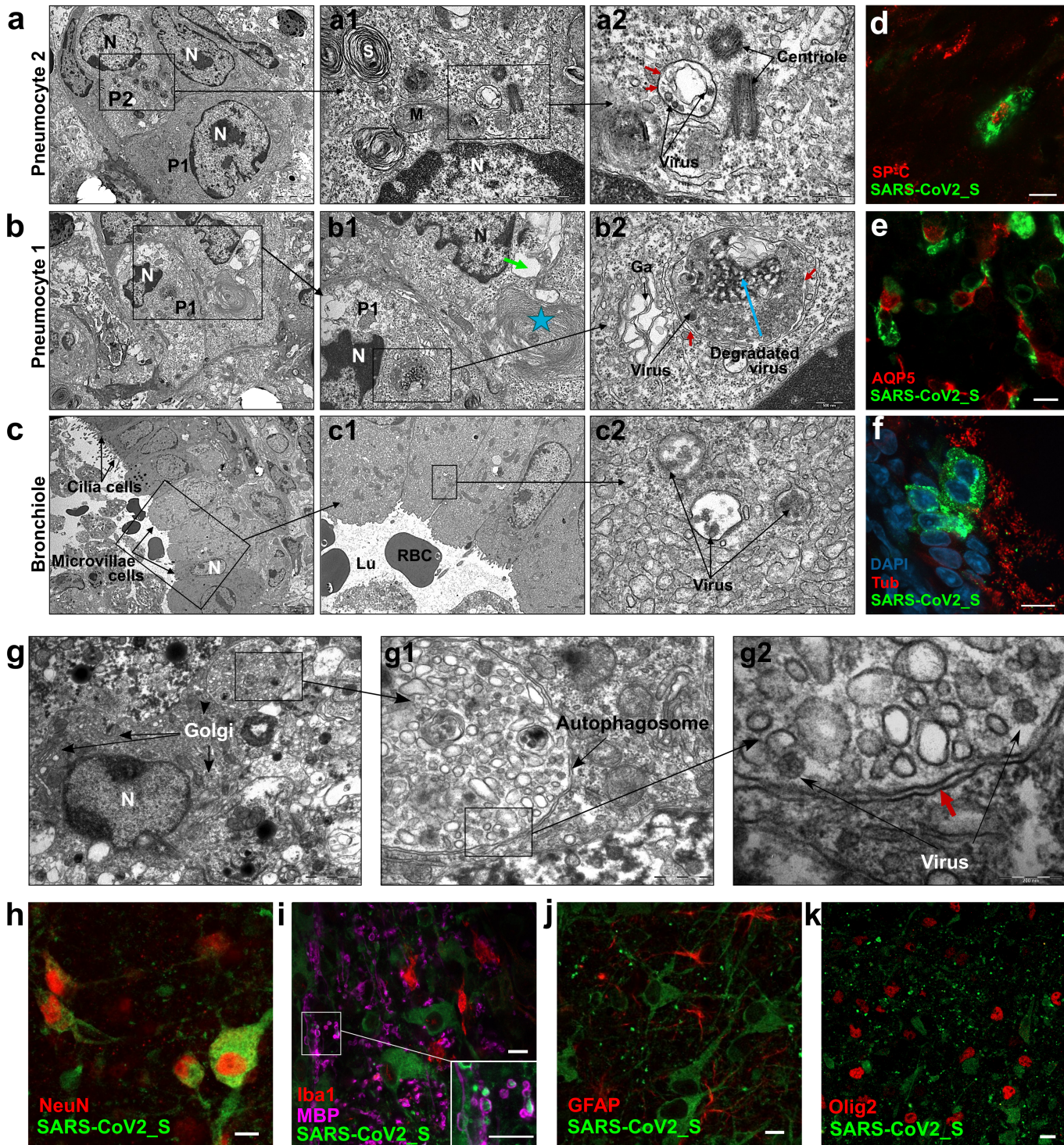


Figure 3

SARS-CoV-2 tropism in hamster lung and brainstem organotypic cultures during the first 2 days of infection. Cultures were infected with 1,000 pfu of SARS-CoV-2 and fixed at day 1 post infection (lung cultures) or 2 days post infection (brainstem cultures). a,b,c, Ultrastructure of infected lung cells by transmission electron microscopy (TEM), scale bar is represented bottom right on each picture. a, Low magnification of lung cells ; P1= type 1 pneumocyte, P2= type 2 pneumocyte, N=nucleus. a1, Enlargement of an infected type 2 pneumocyte with dense lamellar bodies in the cytoplasm (S= surfactant synthesis), a part of the nucleus, the centriole, mitochondria and autophagosomal vacuoles containing virions. a2, High magnification showing the

centriole and the autophagosomal vacuole containing virions. Black arrows point to the double membrane. b, Lung cells undergoing degeneration, displaying vacuoles and degraded cytoplasmic material. N=nucleus, P1= type 1 pneumocyte. b1, Enlargement of cells from the Fig. b, P1 cell contains an autophagosome containing virions, several vacuoles and heterochromatine in the nucleus. The second cell exhibits membrane coiling (star) and large empty vacuoles (green arrow), indicating degradation. b2, High magnification showing the double membrane of the autophagosome (red arrows) containing an accumulation of viral material (blue arrow). The black arrow show viruses surrounding the vacuole. Ga= swelled Golgi apparatus. c, Respiratory bronchiole showing ciliated cells and microvillous cells. N=nucleus. c1, Enlargement of the cells from the Fig. c, showing microvillous cells and red blood cells (RBC) in the lumen of the bronchia (Lu). C2 : High magnification showing three autophagosomes containing virions (arrows). d,e,f, Lung cultures were stained with antibodies: anti-SARS-CoV-2_S, d, anti SP-C, e, anti-AQP5 and f, anti- α acetylated Tubulin (Tub). The immunofluorescence staining analysis was performed by confocal microscopy. Scale bar 10 μ m. g, TEM analysis of a brainstem slice showing an infected neuron with a large Golgi apparatus. g1,2, Enlargement of the autophagosome containing viral particles (white arrows). The double membrane of the autophagosome is pointed with the red arrow. h,i,j,k, Brainstem slices stained with antibodies anti-SARS-CoV-2_S, h, anti-NeuN, i, anti-Myelin Basic Protein (MBP) and Iba1, i, anti-GFAP and j, anti-Olig2. The immunofluorescence staining analysis was performed by confocal microscopy. Scale bar 10 μ m.

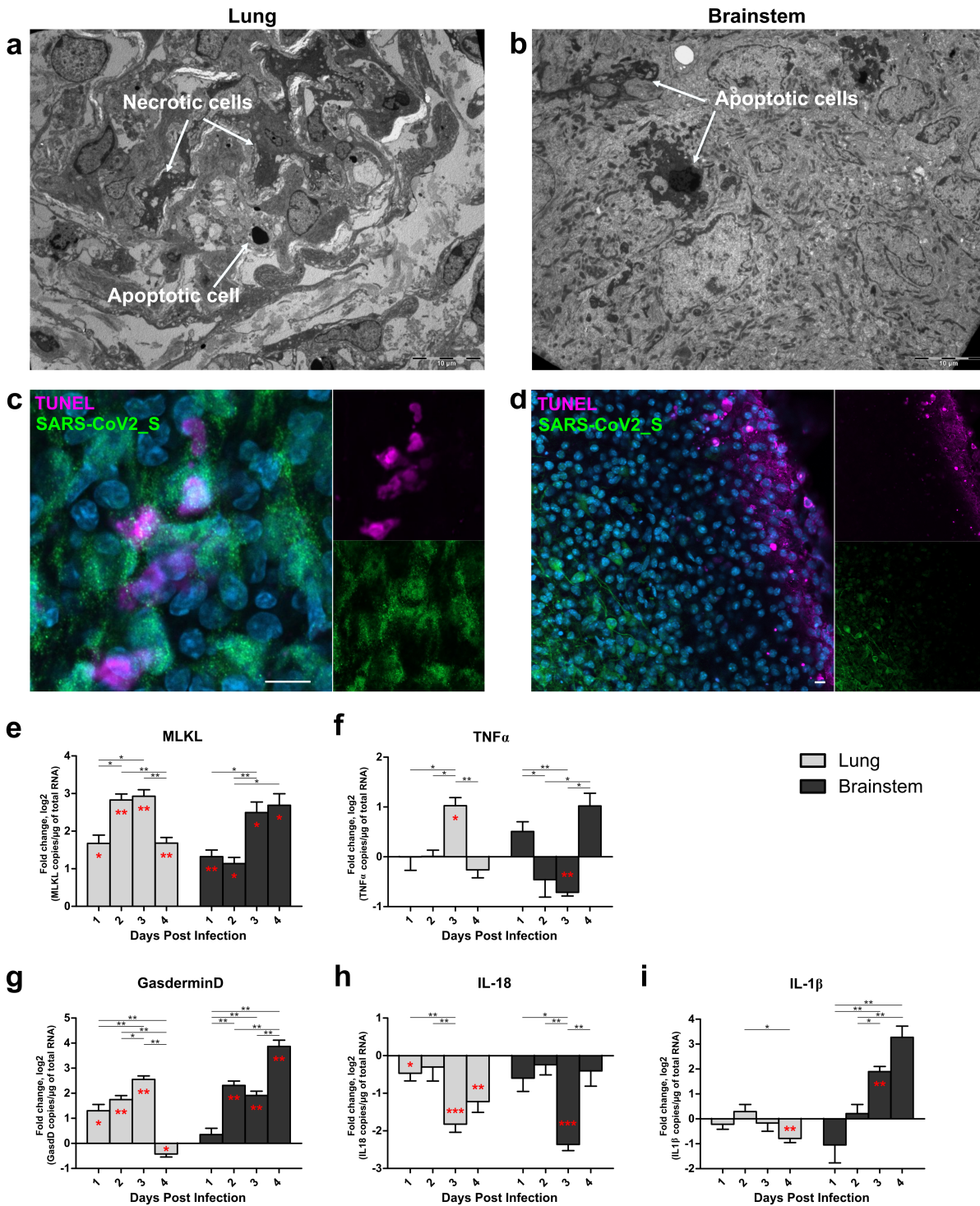


Figure 4

Cell death in the ex vivo cultures. Hamster ex vivo cultures were infected with 1,000 pfu of SARS-CoV-2 (n = 5). a,b,c, Lung and brainstem slices were fixed at 1 day post infection (dpi) or 2 dpi respectively. a,b, Transmission electron microscopy analysis showing necrotic cells and apoptotic cells, scale bar is represented bottom right on each picture. c,d, SARS-CoV-2_S protein immunostaining and TUNEL labelling in the lung and brainstem. Nuclei were counterstained with DAPI. e,f,g,h,i, mRNA expression level of e, MLKL, f, TNF- α , g, Gasdermin D, h, IL-1 β and i, IL-18 over time. mRNA copies per μg of total RNA were quantified by RT-qPCR and normalized to the variation of the amounts of GAPDH mRNA. Fold change are relative to the number of copies of mRNAs in

infected organotypic cultures compared to the uninfected ones. Error bars represent SD. Statistical analyses were performed using the Mann-Whitney test to compare the fold changes between days of culture. mRNA expression level in infected samples were also compared with non-infected samples at the corresponding time point (red stars) using the One sample T-test. *, $P < 0.05$; **, $P < 0.01$; ***, $P < 0.001$.

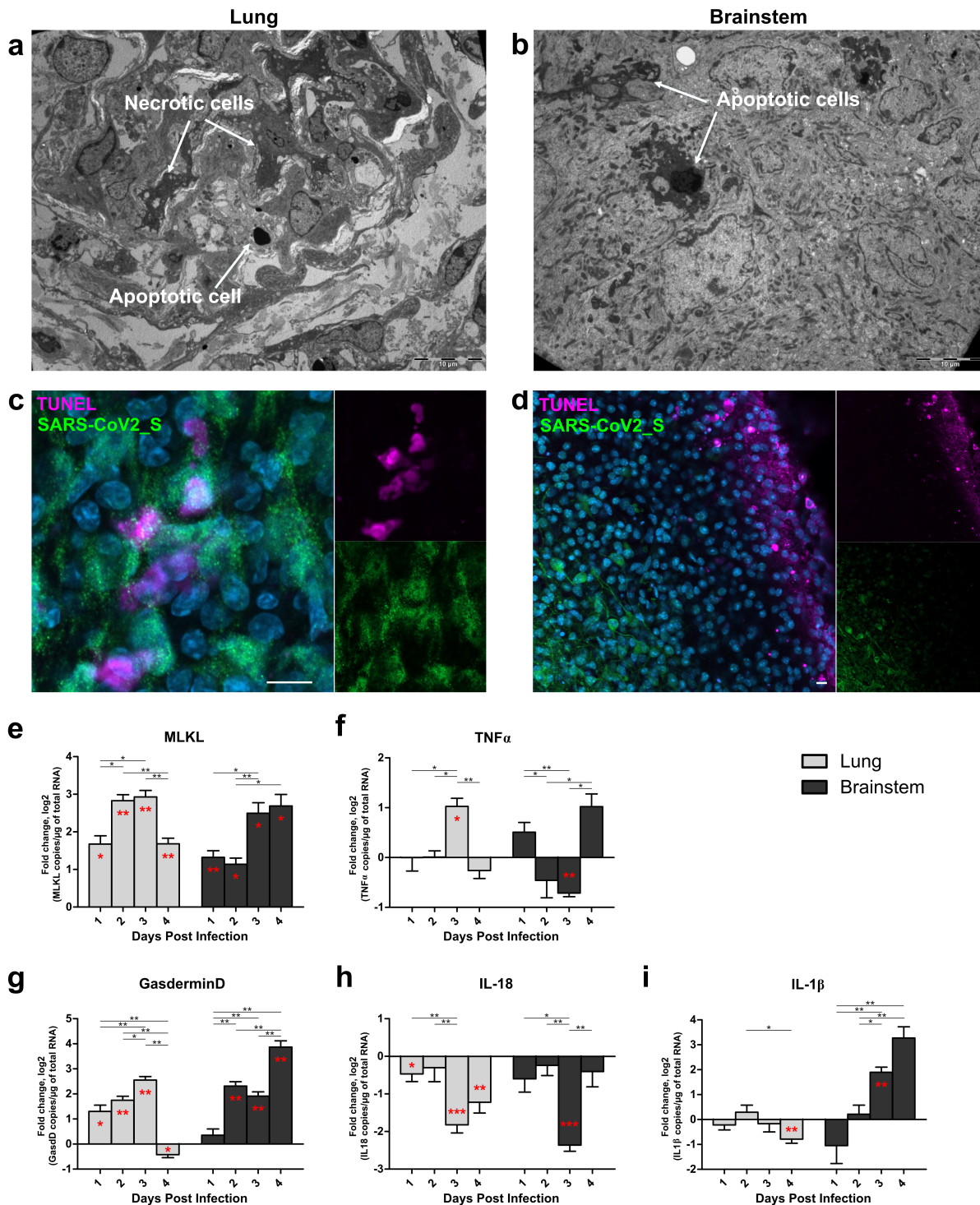


Figure 4

Cell death in the ex vivo cultures. Hamster ex vivo cultures were infected with 1,000 pfu of SARS-CoV-2 (n = 5). a,b,c, Lung and brainstem slices were fixed at 1 day post infection (dpi) or 2 dpi respectively. a,b, Transmission electron microscopy analysis showing necrotic cells and apoptotic cells, scale bar is represented bottom right

on each picture. c,d, SARS-CoV-2_S protein immunostaining and TUNEL labelling in the lung and brainstem. Nuclei were counterstained with DAPI. e,f,g,h,i, mRNA expression level of e, MLKL, f, TNF- α , g, Gasdermin D, h, IL1 β and i, IL-18 over time. mRNA copies per μg of total RNA were quantified by RT-qPCR and normalized to the variation of the amounts of GAPDH mRNA. Fold change are relative to the number of copies of mRNAs in infected organotypic cultures compared to the uninfected ones. Error bars represent SD. Statistical analyses were performed using the Mann-Whitney test to compare the fold changes between days of culture. mRNA expression level in infected samples were also compared with non-infected samples at the corresponding time point (red stars) using the One sample T-test. *, $P < 0.05$; **, $P < 0.01$; ***, $P < 0.001$.

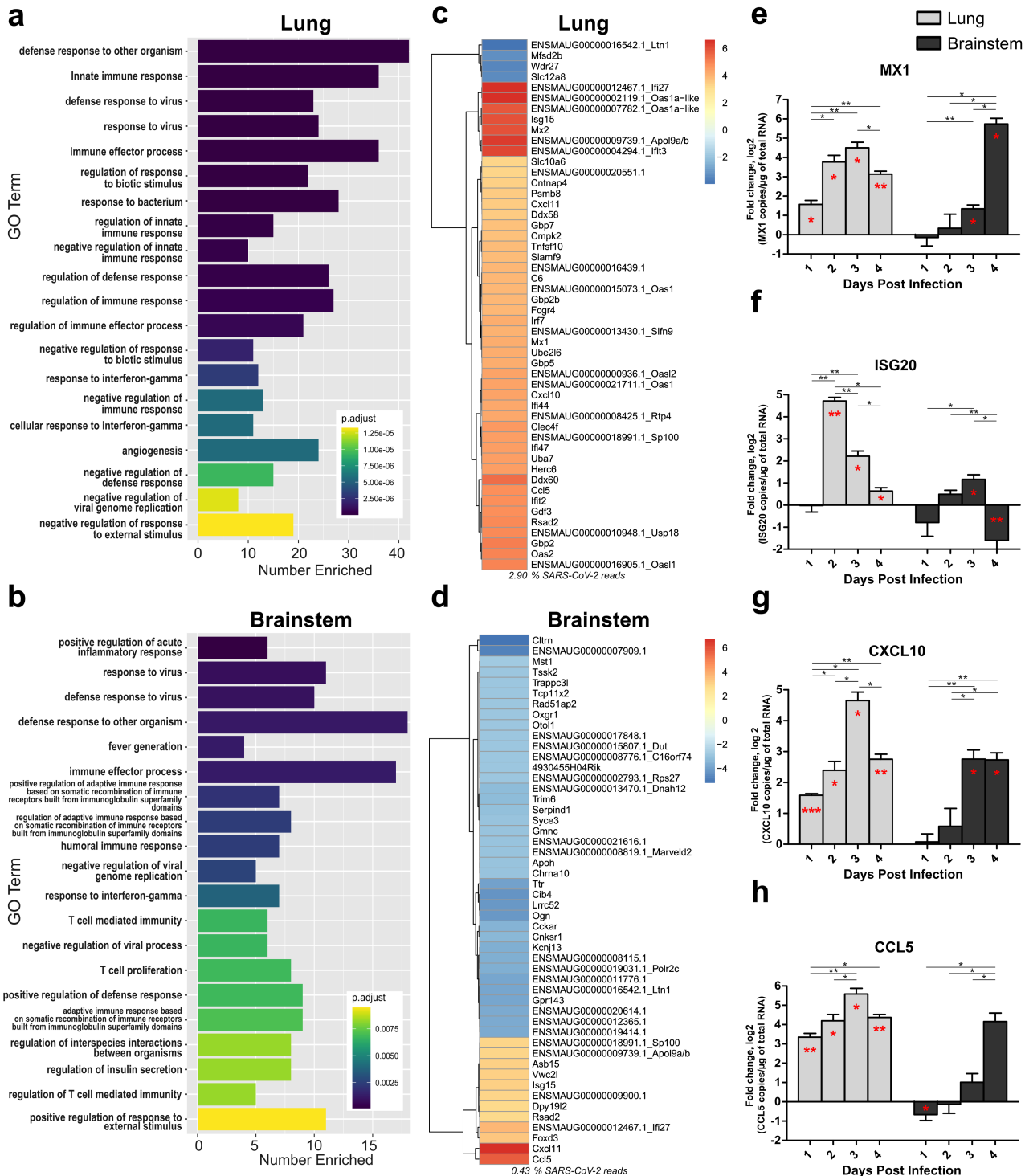


Figure 5

Innate immune transcriptional signature in lung and brainstem organotypic cultures during SARS-CoV-2 infection. Hamster ex vivo cultures were infected with 1,000 pfu of SARS-CoV-2 (n = 5). a,b,c,d, Transcriptomic analysis of the organotypic lung cultures and brainstem cultures 4 days post infection. a,b, Gene Ontology (GO) analysis. For each tissue, the 20 non-redundant GO categories with the lowest adjusted p value for Fisher exact test of enrichment were displayed using ggplot. c,d, Heatmaps generated by calculating the log₂ fold change for infected samples relative to uninfected samples and taking the 50 with the largest absolute value. e,f,g,h, mRNA expression level of e, MX1, f, ISG20, g, CXCL10 and h, CCL5 over time. mRNA copies per µg of total RNA were quantified by RT-qPCR and normalized to the variation of the amounts of GAPDH mRNA. Fold change are relative to the number of copies of mRNAs in infected organotypic cultures compared to the uninfected ones. Error bars represent SD. Statistical analyses were performed using the Mann-Whitney test to compare the fold changes between days of culture. mRNA expression level in infected samples were also compared with non-infected samples at the corresponding time point (red stars) using the One sample T-test. *, P < 0.05; **, P < 0.01; ***, P < 0.001.

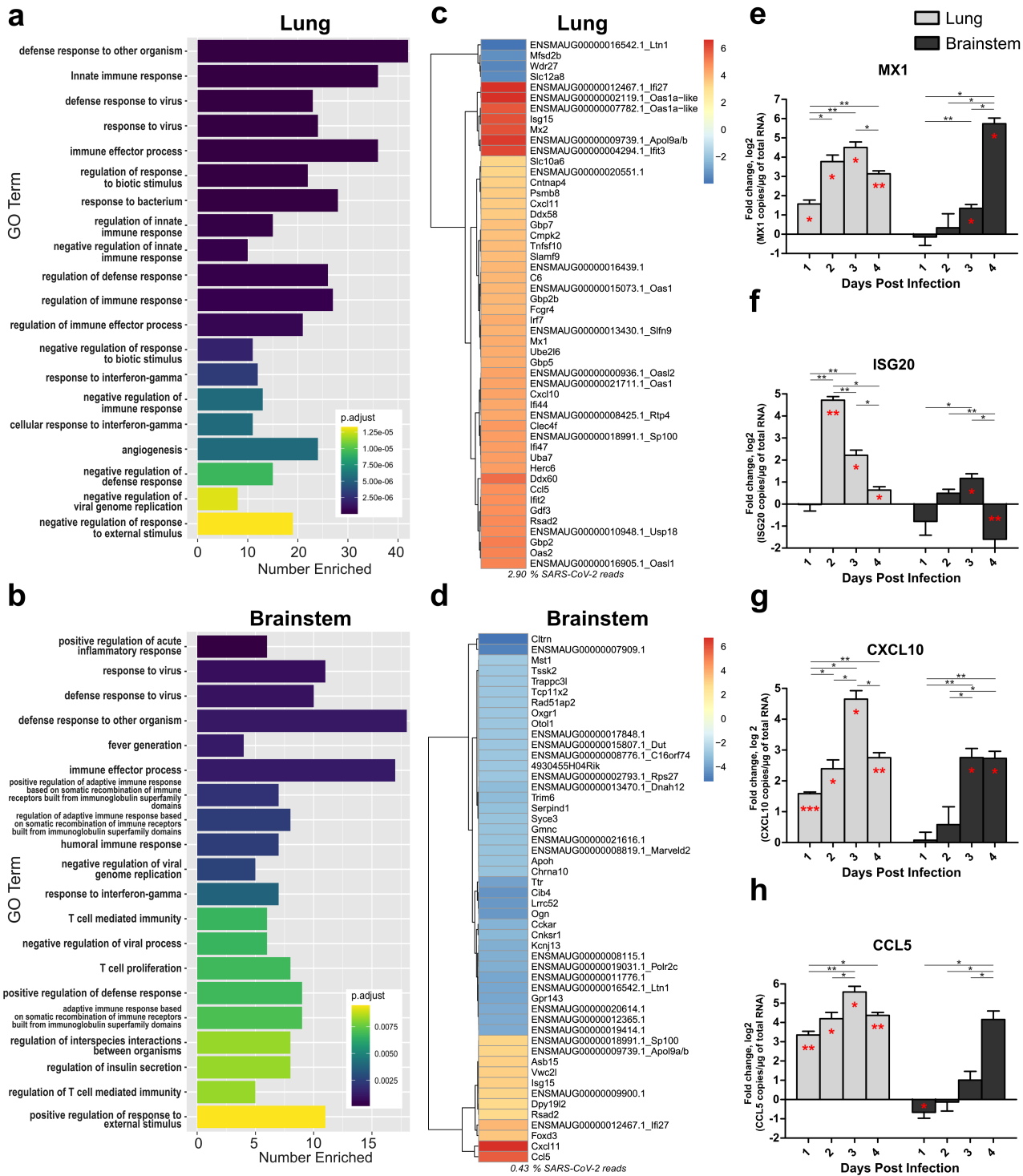


Figure 5

Innate immune transcriptional signature in lung and brainstem organotypic cultures during SARS-CoV-2 infection. Hamster ex vivo cultures were infected with 1,000 pfu of SARS-CoV-2 (n = 5). a,b,c,d, Transcriptomic analysis of the organotypic lung cultures and brainstem cultures 4 days post infection. a,b, Gene Ontology (GO) analysis. For each tissue, the 20 non-redundant GO categories with the lowest adjusted p value for Fisher exact test of enrichment were displayed using ggplot. c,d, Heatmaps generated by calculating the log₂ fold change for infected samples relative to uninfected samples and taking the 50 with the largest absolute value. e,f,g,h, mRNA expression level of e, MX1, f, ISG20, g, CXCL10 and h, CCL5 over time. mRNA copies per μg of

total RNA were quantified by RT-qPCR and normalized to the variation of the amounts of GAPDH mRNA. Fold change are relative to the number of copies of mRNAs in infected organotypic cultures compared to the uninfected ones. Error bars represent SD. Statistical analyses were performed using the Mann-Whitney test to compare the fold changes between days of culture. mRNA expression level in infected samples were also compared with non-infected samples at the corresponding time point (red stars) using the One sample T-test. *, $P < 0.05$; **, $P < 0.01$; ***, $P < 0.001$.

Supplementary Files

This is a list of supplementary files associated with this preprint. Click to download.

- [FigureSupp1.tif](#)
- [FigureSupp1.tif](#)
- [FigureSupp2.tif](#)
- [FigureSupp2.tif](#)